Open-Air Microwave Entanglement Distribution for Quantum Teleportation

Tasio Gonzalez-Raya,[1,2,*] Mateo Casariego,[3,4] Florian Fesquet,[5,6] Michael Renger,[5,6] Vahid Salari,[1,7] Mikko Möttönen,[8,9,10] Yasser Omar,[3,4,11] Frank Deppe,[5,6,12] Kirill G. Fedorov,[5,6] and Mikel Sanz[1,2,13,14,†]

[1] *Department of Physical Chemistry, University of the Basque Country UPV/EHU, Apartado 644, 48080 Bilbao, Spain*

[2] *EHU Quantum Center, University of the Basque Country UPV/EHU, Spain*

[3] *Instituto Superior Técnico, Universidade de Lisboa, Portugal*

[4] *PQI – Portuguese Quantum Institute, Portugal*

[5] *Walther-Meißner-Institut, Bayerische Akademie der Wissenschaften, 85748 Garching, Germany*

[6] *Physik-Department, Technische Universität München, 85748 Garching, Germany*

[7] *Institute for Quantum Science and Technology, University of Calgary, Alberta T2N 1N4, Canada*

[8] *IQM, Keilaranta 19, 02150 Espoo, Finland*

[9] *QCD Labs, QTF Centre of Excellence, Department of Applied Physics, Aalto University, P.O. Box 13500, Aalto FIN-00076, Finland*

[10] *VTT Technical Research Centre of Finland Ltd. & QTF Centre of Excellence, P.O. Box 1000, 02044 VTT, Finland*

[11] *Centro de Física e Engenharia de Materiais Avançados (CeFEMA), Physics of Information and Quantum Technologies Group, Portugal*

[12] *Munich Center for Quantum Science and Technology (MCQST), Schellingstr. 4, 80799 Munich, Germany*

[13] *Basque Center for Applied Mathematics (BCAM), Alameda de Mazarredo 14, 48009 Bilbao, Spain*

[14] *IKERBASQUE, Basque Foundation for Science, Plaza Euskadi 5, 48009 Bilbao, Spain*

(Received 11 April 2022; revised 2 July 2022; accepted 25 July 2022; published 3 October 2022)

Microwave technology plays a central role in current wireless communications, including mobile communication and local area networks. The microwave range shows relevant advantages with respect to other frequencies in open-air transmission, such as low absorption losses and low-energy consumption, and in addition, it is the natural working frequency in superconducting quantum technologies. Entanglement distribution between separate parties is at the core of secure quantum communications. Therefore, understanding its limitations in realistic open-air settings, especially in the rather unexplored microwave regime, is crucial for transforming microwave quantum communications into a mainstream technology. Here, we investigate the feasibility of an open-air entanglement distribution scheme with microwave two-mode squeezed states. First, we study the reach of direct entanglement transmission in open air, obtaining a maximum distance of approximately 500 m with parameters feasible for state-of-the-art experiments. Subsequently, we adapt entanglement distillation and entanglement swapping protocols to microwave technology in order to reduce the environment-induced entanglement degradation. The employed entanglement distillation helps to increase quantum correlations in the short-distance low-squeezing regime by up to 46%, and the reach of entanglement increases by 14% with entanglement swapping. Importantly, we compute the fidelity of a continuous-variable quantum teleportation protocol using open-air-distributed entanglement as a resource. Finally, we adapt this machinery to explore the limitations of quantum communication between satellites, where the impact of thermal noise is substantially reduced and diffraction losses are dominant.

DOI: 10.1103/PhysRevApplied.18.044002

[*] tasio.gonzalez@ehu.eus
[†] mikel.sanz@ehu.eus

I. INTRODUCTION

Quantum communication [1–3] represents an application of quantum information theory that tackles the subject of information transfer by taking advantage of purely quantum resources, such as superposition and entanglement. By establishing quantum channels to share quantum resources, namely quantum states, as well as secure classical channels, it aims at outperforming classical communication protocols in both efficiency and security.

Among the best-known quantum communication protocols, quantum teleportation [4,5] aims at transferring information of an unknown quantum state held by one party, to a second party at a remote location, by means of an entangled resource and classical communication. Initially proposed for discrete-variable quantum states [6,7], this protocol has also been studied in continuous-variable settings [8–10].

Another notorious advantage of quantum communication is quantum key distribution [11,12], whose foundation has been set by two distinct protocols: BB84 [13] and E91 [14]. These protocols allow two distant parties to develop a shared random key, which is unconditionally secure against eavesdroppers by virtue of quantum laws.

At the heart of many quantum communication protocols lies entanglement distribution [15–18], also a key point for the famous quantum internet idea [19–21]; quantum entanglement distribution represents the act of sharing entangled states between communication parties. This has been experimentally attained [22–24], as well as quantum key distribution [25–27] and quantum teleportation [28–33], through optical fibers and through open air.

The subject of quantum communication has been developed parallel to other areas such as quantum computing, quantum sensing [34,35], or quantum metrology [36,37], to which it is usually tangential. Quantum computing, for example, is expected to benefit from efficient transfer of quantum information between processing units, a proposal that is categorized as distributed quantum computing [38,39]. Quantum sensing and quantum metrology profit from the use of entanglement in their attempt to perform high-resolution measurements on various systems. By using quantum resources, they can reach ultimate measurement limits set by quantum mechanics, thus outperforming classical strategies. Respective examples can be found in the detection of gravitational waves at LIGO [40,41], in the measurement of biological systems [42,43], quantum imaging [44,45], navigation [46], and synchronization [47], among others.

The flourishing of these quantum-information-based fields has gone hand in hand with the development of quantum technologies, among which superconducting circuits stand out in terms of controllability, scalability, and coherence. Partially, this is due to the development of Josephson junctions (JJs) [48], nonlinear elements with essential applications in quantum computation [49–51], and quantum information processing [52,53]. This has led to different experiments in quantum state transfer and remote entanglement preparation between various JJ-based superconducting devices [54–61], as well as to sensitive noise analysis [62,63]. These devices naturally work at microwave frequencies (1–100 GHz), for which the number of thermal photons per mode at room temperature ($T = 300$ K) is around 1250 at 5 GHz, thus creating the need for cryogenic cooling in order to shield superconducting circuits from thermal noise. This problem is somewhat nonexisting in the optical regime, where most quantum communication experiments have been performed so far. However, in this regime there are many other sources of error and inefficiency [64]: large absorption losses in open air and significant power consumption requirements. At the same time, in order to establish a quantum communication channel between superconducting quantum circuits, one requires either converting microwave photons to the optical domain [65,66] or using microwave quantum signals directly. The former approach still suffers from huge conversion quantum inefficiencies of the order of 10^{-5}. Therefore, it is natural to consider the purely microwave quantum communication approach, its advantages, and limitations.

Another interesting application of the Josephson junction is the Josephson parametric amplifier (JPA), a device that can generate squeezed states [67], from which entangled resources [68,69] can be produced for quantum communication with microwaves. Among the various applications of open-air entanglement distribution, quantum teleportation represents one of the fundamental quantum communication protocols, since its associated network has just two nodes: Alice and Bob. This protocol has been explored in the microwave cryogenic environment, both theoretically [70] and experimentally [10]. However, a realistic model for open-air quantum teleportation with microwaves should take into account additional challenges associated with impedance mismatches and absorption losses in order to find ways to mitigate these imperfections.

In this article, we address two pragmatic questions: which is the maximum distance for open-air microwave Gaussian entanglement distribution in a realistic scenario, and which technological and engineering challenges remain to be faced? In particular, we adapt the Braunstein-Kimble quantum teleportation protocol employing entangled resources previously distributed through open air, adapted to microwave technology. Performing this protocol is possible due to the recent breakthrough in the development of microwave homodyning [10] and photocounting [71] schemes. When formulated in continuous variables, teleportation assumes a previously shared entangled state, ideally a two-mode squeezed vacuum (TMSV) state with infinite squeezing. In real life, however, only a finite squeezing level can be produced, making the state

sensitive to entanglement degradation whenever either one or both modes are exposed to decoherence processes like thermal noise and/or photon losses. As the thermal microwave background in space is smaller, we investigate the distances for entanglement preservation in microwave quantum communication between satellites. Based on previous works [72,73], we neglect environmental attenuation and focus on diffraction losses, a powerful loss mechanism in microwaves. The article is organized as follows. In Sec. II, we introduce the main concepts in quantum continuous variables, which are needed for describing quantum microwaves, and briefly discuss the quantum teleportation protocol of Braunstein and Kimble [8]. In Sec. III, we study the generation of two-mode squeezed states and the challenges of their subsequent distribution through open air, and compute maximum distances of entanglement preservation for various physical situations. In Sec. III C, we review entanglement distillation and entanglement swapping techniques for reducing the effects of noise and losses in open air. In Sec. IV we consider recent advances in microwave photodetection and homodyning, and address their current limitations. In Sec. V, we investigate open-air microwave quantum teleportation fidelities using the various quantum states derived in the manuscript, and we conclude by addressing the same concerns in quantum communication between satellites in Sec. VI.

II. QUANTUM CONTINUOUS-VARIABLE FORMALISM

A. Review of Gaussian states

When some degree of freedom of a quantum system is described by a continuous-spectrum operator, we say that it is a "continuous variable" (CV). Bosonic CV states are those whose quadratures (or, equivalently, their creation and annihilation operators) have a continuous spectrum or, equivalently, the complete description of the Hilbert space requires an infinite-dimensional basis (typically, the Fock basis). Gaussian states are CV states associated with Hamiltonians that are, at most, quadratic in the field operators. As such, their full description does not require the infinite-dimensional density matrix, and can be compressed into a vector and a matrix, called the displacement vector and the covariance matrix, respectively. These are related to the first and second moments of a Gaussian distribution; hence, their name "Gaussian states". For a system with density matrix ρ describing N distinguishable modes, or particles, the displacement vector $\mathbf{d}$ is a $2N$ vector and the covariance matrix Σ is a $2N \times 2N$ square matrix:

$$\mathbf{d} := \mathrm{tr}[\rho \hat{\mathbf{r}}], \tag{1}$$

$$\Sigma := \mathrm{tr}[\rho\{(\hat{\mathbf{r}} - \mathbf{d}), (\hat{\mathbf{r}} - \mathbf{d})^{\intercal}\}]. \tag{2}$$

Here $\hat{\mathbf{r}} := (\hat{x}_1, \hat{p}_1, \hat{x}_2, \hat{p}_2, \ldots, \hat{x}_N, \hat{p}_N)$ defines the so-called "real basis", for which canonical commutation relations read $[\hat{\mathbf{r}}, \hat{\mathbf{r}}^{\intercal}] = i\Omega$, where $\Omega = \bigoplus_{j=1}^{N} \Omega_1$ is the quadratic (or symplectic) form, and

$$\Omega_1 = \begin{pmatrix} 0 & 1 \\ -1 & 0 \end{pmatrix}, \tag{3}$$

where we have chosen natural units, $\hbar = 1$. Note that the *canonical* position and momentum operators are defined by the choice $\kappa = 2^{-1/2}$ in $\hat{a}_j = \kappa(\hat{x}_j + i\hat{p}_j)$.

The normal mode decomposition theorem [74], which follows from Williamson's seminal work [75–77], can be stated as every positive-definite Hermitian matrix Σ of dimension $2N \times 2N$ can be diagonalized with a symplectic matrix S: $D = S\Sigma S^{\intercal}$ with $D = \mathrm{diag}(\nu_1, \nu_1, \ldots, \nu_N, \nu_N)$, where the ν_a, for $a \in \{1, \ldots, N\}$, are the symplectic eigenvalues of Σ, defined as the positive eigenvalues of matrix $i\Omega\Sigma$. A Gaussian state satisfies $\nu_a \geq 1$, with equality for all a strictly for the pure state case (which meets $\det\Sigma = 1$). As a measure of bipartite, mixed state entanglement, the negativity is the most commonly used entanglement monotone, and is defined as $2\mathcal{N}(\rho) := \|\tilde{\rho}\|_1 - 1$, where $\|\tilde{\rho}\|_1 := \mathrm{tr}\sqrt{\tilde{\rho}^{\dagger}\tilde{\rho}}$ is the trace norm of the partially transposed density operator. In general, $\mathcal{N}(\rho) = \left|\sum_j \lambda_j\right|$ with the λ_j the negative eigenvalues of $\tilde{\rho}$. For a bipartite Gaussian state with covariance matrix

$$\Sigma = \begin{pmatrix} \Sigma_A & \varepsilon_{AB} \\ \varepsilon_{AB}^{\intercal} & \Sigma_B \end{pmatrix}, \tag{4}$$

one defines the two partially transposed symplectic eigenvalues as

$$\tilde{\nu}_{\mp} := \sqrt{\frac{\tilde{\Delta} \mp \sqrt{\tilde{\Delta}^2 - 4\det\Sigma}}{2}}, \tag{5}$$

where the partially transposed symplectic invariant is $\tilde{\Delta} = \det\Sigma_A + \det\Sigma_B - 2\det\varepsilon_{AB}$. The negativity can then be obtained as

$$\mathcal{N}(\rho) = \max\left\{0, \frac{1 - \tilde{\nu}_-}{2\tilde{\nu}_-}\right\}. \tag{6}$$

Hence, a bipartite Gaussian state is separable when the smaller partially transposed symplectic eigenvalue meets the condition $\tilde{\nu}_- \geq 1$. Alternatively, it is entangled when $\tilde{\nu}_- < 1$ is met.

Coherent states $\{|\alpha\rangle\}_{\alpha\in\mathbb{C}}$ are defined as the eigenstates of the annihilation operator $\hat{a}$ with eigenvalue $\sqrt{2}\alpha = x + ip$, where $x, p \in \mathbb{R}$ are the eigenvalues of the canonical position and momentum operators, respectively. They play an important role in quantum CVs, as they allow for a straightforward phase

space description of Gaussian states. The displacement operator $\hat{D}_{-\mathbf{d}} := \exp[-i\mathbf{d}\Omega_1\hat{\mathbf{d}}^\intercal] = \hat{D}_\alpha = \exp[\alpha\hat{a}^\dagger - \bar{\alpha}\hat{a}]$ acts on the vacuum as $\hat{D}_\alpha\,|0\rangle = |\alpha\rangle$, and satisfies $\hat{D}_\alpha^\dagger = \hat{D}_{-\alpha}$. Coherent states are not orthogonal, and their overlap can be computed as $\langle\beta|\alpha\rangle = \exp[-(\alpha\bar{\beta} - \bar{\alpha}\beta - |\alpha-\beta|^2)/2]$. This does not prevent the set of all coherent states from forming a basis, which, though overcomplete, allows one to find the coherent states resolution of the identity, $\mathbb{1} = \pi^{-1}\int \mathrm{d}^2\,\alpha\,|\alpha\rangle\,\langle\alpha|$, where $\mathrm{d}^2\,\alpha \equiv \mathrm{d}\,\mathrm{Re}\{\alpha\}\,\mathrm{d}\,\mathrm{Im}\{\alpha\}$, enabling the computation of traces of operators in an integral fashion: $\mathrm{tr}[\hat{O}] = \pi^{-1}\int \mathrm{d}^2\,\alpha\,\langle\alpha|\,\hat{O}\,|\alpha\rangle$. In this context, it is common to use the fact that, for a coherent state $\mathbf{d} = (x,p) = \sqrt{2}(\mathrm{Re}\{\alpha\},\mathrm{Im}\{\alpha\})$, and so $2\,\mathrm{d}^2\,\alpha = \mathrm{d}\,x\,\mathrm{d}\,p$. More generally, an n-mode displacement operator may be defined via $\hat{D}_{-\mathbf{d}} = \bigotimes_{j=1}^n \hat{D}_{-\mathbf{d}_j} = \hat{D}_{-\bigoplus_{j=0}^n \mathbf{d}_j}$, where $\mathbf{d}_j := (x_j, p_j)$, and $\Omega := \bigoplus_{j=1}^n \Omega_1$. A complete representation of states that is closely related to coherent states is given by the (Wigner) characteristic function, normally referred to simply as the characteristic function (CF), and for an n-mode state ρ (not necessarily Gaussian), is given by

$$\chi(\mathbf{d}) = \mathrm{tr}[\rho\hat{D}_{-\mathbf{d}}] \tag{7}$$

with normalization condition given by $\chi(\mathbf{0}) = 1$. A Gaussian state of first and second moments $(\mathbf{d}, \Sigma)$ has a CF given by

$$\chi_G(\mathbf{r}) = e^{-\mathbf{r}\Omega\Sigma\Omega^\intercal\mathbf{r}^\intercal/4}e^{-i\mathbf{r}\Omega\mathbf{d}^\intercal}, \tag{8}$$

where $\mathbf{r} = (x_1, p_1, \ldots, x_N, p_N) \in \mathbb{R}^{2N}$.

B. Quantum teleportation with CVs

Quantum teleportation is a quantum communication protocol that, in principle, allows one to achieve perfect transfer of quantum information between two parties by means of previously shared entanglement, combined with local operations and classical communication. The protocol was first proposed in 1993 by Bennett and collaborators [4], as a way to take advantage of an entangled resource for the task of sending an unknown quantum state from one place to another, using discrete-variable quantum states. The original idea was simple, yet powerful: assuming that a maximally entangled, bipartite Bell state was shared between two parties (Alice and Bob) prior to the start of the protocol, Alice, in possession of some *unknown* state $|\psi\rangle = \alpha\,|0\rangle + e^{i\beta}\sqrt{1-|\alpha|^2}\,|1\rangle$ couples her part of the Bell state to $|\psi\rangle$ by means of a Bell measurement, whose 2-bit output she communicates classically to Bob. Upon receiving the message, Bob performs a conditional unitary on his part of the shared Bell state, recovering $|\psi\rangle$ modulo a global phase in his location.

A year later, Vaidman extended the idea to the transmission of a CV state by means of a perfectly correlated (singular) position-momentum EPR state shared by Alice and Bob [78]. In 1998, Braunstein and Kimble [8] made this idea more realistic by relaxing the correlation condition to more experimentally accessible states, such as finitely squeezed states. Their protocol, known as the Braunstein-Kimble protocol, was first realised in 1998 by Furusawa *et al.* in the optical domain [29]. We review the protocol here for convenience.

Kimble and Braunstein derived an expression for fidelity between an unknown state of a single-mode Bosonic field and a teleported copy, when imperfect quantum entanglement is shared between the two parties. A generalization to a broadband version, where the modes have finite bandwidths, followed quite directly [79]. In the Braunstein-Kimble protocol, Alice and Bob share a TMSV state, which enables them to teleport the complete state of a single mode of the electromagnetic field, where two orthogonal field quadratures play the role of position and momentum. Shortly after, quantum teleportation of an unknown coherent state was demonstrated, showing an average fidelity [see Eq. (13) below] $\overline{F} = 0.58 \pm 0.02$ [29], which beat the maximum classical fidelity of $\overline{F} = 0.5$ for Gaussian states [79–81]. Other works followed, where the Bell measurement of two orthogonal quadratures was replaced by the photon-number difference and phase sum, and the question of an optimal quantum teleportation protocol depending on the entangled resource was raised [82]. Subtraction of single photons from TMS states has been shown to enhance the fidelity of teleportation [83,84]. We review here the Braunstein-Kimble protocol, replacing the Wigner function approach with its Fourier transform, the characteristic function. The protocol is as follows.

1. Alice uses a 50:50 beam splitter to couple her part of the resource state ρ_{AB} with an incoming unknown state ρ_T^{in}. The output Hilbert spaces of this beam splitter are labeled A and T.
2. Alice performs two homodyne detections, where each of the local oscillator phases are set in order to measure photocurrents, whose differences are integrated over some time, and proportional to quadratures $\hat{x}_T := (\hat{x}_1 + \hat{x}_{\mathrm{in}})/\sqrt{2}$ and $\hat{p}_A := (\hat{p}_1 - \hat{p}_{\mathrm{in}})/\sqrt{2}$. She sends the outcomes (x_T, p_A) to Bob via a classical communication channel.
3. Bob, upon reception of the signal (x_T, p_A), performs a displacement $\hat{D}(\xi)$ to his part of ρ_{AB}, with $\xi := (x_T + ip_A)/\sqrt{2}$. The state at Bob's location is now, in average, closer to ρ_{in} than what it would be if no entanglement was present in ρ_{AB}.

This protocol is depicted in Fig. 1, where we also sketch the sequence that leads to an entangled resource shared through open air by Alice and Bob, which is then consumed in the teleportation process. For simplicity, we define $(x_T, p_A) = (x, p)$. The conditional state that Bob has after knowing the outcomes of Alice's homodyne measurements is

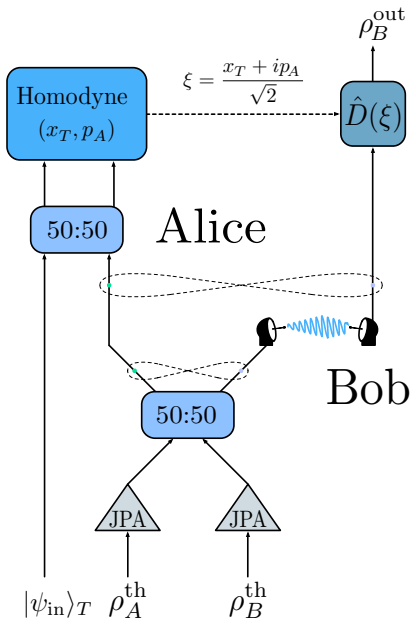

FIG. 1. Circuit representation of a CV microwave quantum teleportation protocol with Gaussian states. The entangled resource is harvested from two single-mode squeezed thermal states, generated from identical JPAs, which are then combined on a balanced beam splitter. Assuming that this state is generated by Alice, one of the modes has to be sent to Bob, represented here by the presence of antennae, in order for the two parties to share the entangled resource. Following this, Alice combines the target state to be teleported $|\psi_{\text{in}}\rangle_T$ with the mode of the entangled state she holds in a balanced beam splitter, which is then subject to two homodyne detections, x_T and p_A. The measurement results ξ are communicated to Bob, who applies a displacement $\hat{D}(\xi)$ on his part of the entangled resource, resulting in the state ρ_B^{out}.

$$\rho_B(x,p) = \frac{1}{P_B(x,p)} \langle \Pi(x,p)|\rho_T^{\text{in}} \otimes \rho_{AB}|\Pi(x,p)\rangle_{TA} \quad (9)$$

with $P_B(x,p) = \text{tr}_B\langle \Pi(x,p)|\rho_{\text{in}} \otimes \rho_{AB}|\Pi(x,p)\rangle_{TA}$ and

$$|\Pi(x,p)\rangle_{TA} = \frac{1}{\sqrt{2\pi}} \int_{\mathbb{R}} \text{d}y e^{ipy} |x+y\rangle_T |y\rangle_A, \quad (10)$$

which is an element of the maximally entangled basis corresponding to Alice's Bell-like measurement. Now, this expectation value over the teleported (T) and the senders' (A) modes is computed as

$$\begin{aligned} &\langle \Pi(x,p)|\rho_{\text{in}} \otimes \rho_{AB}|\Pi(x,p)\rangle_{TA} \\ &= \frac{1}{2\pi} \int_{-\infty}^{\infty}\int_{-\infty}^{\infty} \text{d}y\, \text{d}y' e^{ip(y-y')} \\ &\quad \times \langle x+y'|\rho_{\text{in}}|x+y\rangle_T \langle y'|\rho_{AB}|y\rangle_A. \end{aligned} \quad (11)$$

Once we have computed $\rho_B(x,p)$, we need to compute the outcoming state after the receiver applies the displacements, and average over all possible measurement outcomes:

$$\rho_B^{\text{out}} = \int_{-\infty}^{\infty} \text{d}x \int_{-\infty}^{\infty} \text{d}p P_B(x,p) \hat{D}_B(\xi) \rho_B(x,p) \hat{D}_B^\dagger(\xi). \quad (12)$$

As a measure of the quality of the protocol, one typically uses an overlap fidelity $F(\rho_{\text{in}}, \rho_{\text{out}}) = \text{tr}[\rho_{\text{in}}\rho_{\text{out}}]$, which represents a simplified version of the Uhlmann fidelity $(\text{tr}[\sqrt{\sqrt{\rho_{\text{in}}}\rho_{\text{out}}\sqrt{\rho_{\text{in}}}}])^2$ in the case when ρ_{in} is pure.

The figure of merit in quantum teleportation is the *average* fidelity, which refers to the fact that we have averaged over all possible measurement outcomes,

$$\overline{F} = \text{tr}[\rho_T^{\text{in}} \rho_B^{\text{out}}]. \quad (13)$$

Sometimes it can be useful to have it written in terms of the CFs [85]:

$$\overline{F} = \frac{1}{\pi} \int \text{d}^2\beta\, \chi_T^{\text{in}}(-\beta)\chi_B^{\text{out}}(\beta) \quad (14)$$

with the average over (x,p) having already been performed in ρ_B^{out}.

If the resource state ρ_{AB} is a Gaussian state with the covariance matrix given in Eq. (4), and the teleported state is a coherent state $|\alpha_0\rangle\langle\alpha_0|$, the average fidelity can be written as

$$\overline{F} = \frac{1}{\sqrt{\det[\mathbb{1}_2 + \Gamma/2]}} \quad (15)$$

with $\Gamma \equiv (\sigma_Z \Sigma_A \sigma_Z + \Sigma_B - \sigma_Z \varepsilon_{AB} - \varepsilon_{AB}^{\intercal}\sigma_Z)$. Coherent states are typically those chosen to be teleported due to the ease of their experimental generation. In theory, the result of the average fidelity does not depend on the displacement α_0; therefore, it will suffice to use an unknown coherent state for a demonstration of quantum teleportation. In experiments, however, the teleportation fidelity may depend on α_0.

It is also interesting to see the average fidelity of a process in which k teleportation protocols are concatenated, i.e.,

$$\overline{F}^{(k)} = \frac{1}{\sqrt{\det[\mathbb{1}_2 + (k-1/2)\Gamma]}}, \quad (16)$$

assuming that, in each step, an entangled Gaussian resource with the covariance matrix that characterizes Γ is used.

Consider a symmetric covariance matrix with $\Sigma_A = \Sigma_B = \alpha\mathbb{1}_2$ and $\varepsilon_{AB} = \gamma\sigma_z$. Then, we have $\Gamma = 2(\alpha - \gamma)\mathbb{1}_2$ and $\tilde{\nu}_- = \alpha - \gamma$, which leads to

$$\overline{F} = \frac{1}{1 + \tilde{\nu}_-}. \quad (17)$$

It is easy to check the two following limits for the average teleportation fidelity of an arbitrary coherent state:

$\lim_{\tilde{\nu}_- \to 1} \overline{F} = 1/2$ and $\lim_{\tilde{\nu}_- \to 0} \overline{F} = 1$. The first limit corresponds to using no entanglement ($\tilde{\nu}_- \geq 1$), and is interpreted as the "classical teleportation" threshold, meaning that any approach giving an average fidelity of 0.5 or less does not demonstrate quantum teleportation. The second limit corresponds to an idealized case of an infinite two-mode squeezing level ($\tilde{\nu}_- = 0$), i.e., an EPR state, which realizes perfect quantum teleportation.

III. OPEN-AIR MICROWAVE ENTANGLEMENT DISTRIBUTION

The scheme we have envisioned (see Fig. 2) for open-air entanglement distribution relies on a variety of things: first, generation of two-mode squeezed thermal (TMST) states with thermal photons $n < e^{-r}\sinh(r)$, given squeezing r, which will take place in a cryostat at $T \sim 50$ mK temperatures; second, efficient transmission of states out of the cryostat and into open air, targeting optimal entanglement preservation; for this task, we rely on an antenna based on the design proposed in Ref. [86] with special attention given to the shape of the impedance function, which greatly affects entanglement preservation; third, estimation of losses in open air that describe the attenuation of the signal caused by the presence of thermal noise in the environment, with the objective of setting bounds on effective transmission distances. This protocol will prepare the foundation for an open-air microwave quantum teleportation protocol, whose fidelity will depend on the entanglement of the resource shared by the parties involved.

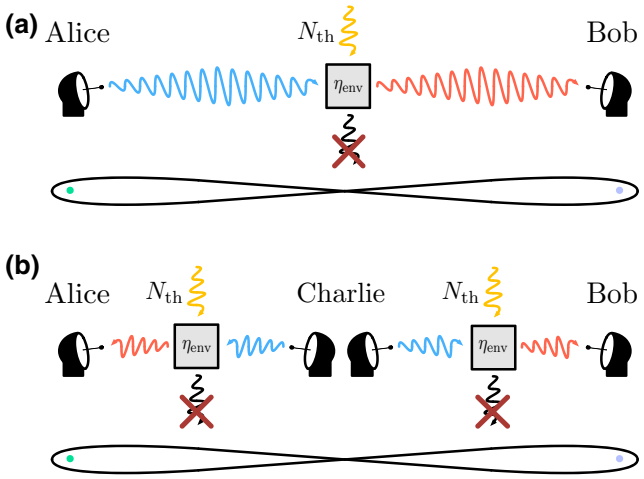

FIG. 2. Representation of an entanglement distribution protocol that uses antennae to efficiently transmit the quantum states into open air, where photon losses and thermal noise effects are described with a beam splitter with reflectivity $\eta_{\rm env}$. We analyze two different scenarios: (a) Alice generates the entangled state, and attempts to share one of its modes with Bob by sending it through a noisy and lossy open-air channel that degrades the entanglement strength; (b) Charlie generates a two-mode entangled state, and sends one entangled mode to Alice and another to Bob. In this case, although both modes go through the same noisy and lossy channel, they travel half the distance compared to the previous case.

A. State generation

As the first step, we discuss the generation of entangled states inside a cryostat, more precisely, two-mode squeezed states. Squeezing is an operation in which one of the variances of the electromagnetic field quadratures of a quantum state is reduced below the level of vacuum fluctuations, while the conjugate quadrature is amplified, satisfying the uncertainty principle. This can be achieved by sending the vacuum state to a JPA, a coplanar waveguide resonator line terminated by a direct-current superconducting quantum interference device (dc SQUID). The dc SQUID provides magnetic flux tunability to the resonator and enables parametric phase-sensitive amplification, which is the key for generating squeezed microwave states [87,88].

The relation between the frequency of the external magnetic flux, Ω, and the fundamental frequency of the JPA, ω_c, determines whether the JPA operates in the phase-insensitive or phase-sensitive regime. The latter is achieved in the so-called degenerate regime, $\Omega = 2\omega_c$. A corresponding three-wave mixing process, when one pump photon splits into two signal photons, is described by the Hamiltonian

$$H = g\left(\beta^* a^2 - \beta a^{\dagger 2}\right). \tag{18}$$

It can be shown that the aforementioned Hamiltonian corresponds to a single-mode squeezing operator

$$S(\xi) = \exp\left[\tfrac{1}{2}\left(\xi^* a^2 - \xi a^{\dagger 2}\right)\right], \tag{19}$$

with the squeezing parameter given by $|\xi| \propto 2g|\beta|t$.

A symmetric two-mode squeezed state can be generated by combining two, orthogonally squeezed, states with equal squeezing levels at a hybrid ring. The latter element represents a symmetric 50:50 microwave beam splitter. Microwave squeezed states produced by JPAs are subject to various sources of imperfections and noise. Therefore, the output states can be effectively modeled as two-mode squeezed thermal states, whose second moments differ from those of ideal two-mode squeezed vacuum states by a factor of $1 + 2n$, where n is the number of thermal photons.

Thermal photons in squeezed states may have various physical origins. One of the most trivial reasons for noise in the two-mode squeezed states is finite temperatures of the input JPA modes, which lead to the fact that one applies a squeezing operator to a thermal state rather than to a vacuum. Another important source of noise in squeezed states produced by flux-driven JPAs arises from Poisson photon-number fluctuations in the pump mode, which lead

to extra quasithermal photons in the output squeezed states [89]. Last but not least, higher-order nonlinear effects also contribute to additional effective noise under the Gaussian approximation [90]. More experimental details on the microwave squeezing and related imperfections can be found elsewhere [69].

B. Antenna model and open-air losses

In transmission of quantum states from a cryostat into the open air, an interface antenna comes into play as an inhomogeneous medium (as depicted in Fig. 3) that connects those two very different environments. The main purpose of this antenna is to maximize transmission of the incident signal to the open-air medium. Here, we consider a transmission line coming out of the cryostat with an impedance of 50 Ω, and assume focused transmission in open air described by a transmission line with impedance 377 Ω. Such an antenna can be modeled by a finite transmission line with variable characteristic impedance and designed to match the impedances of the cryostat and of open air at its ends. This approach was discussed in a previous study [86], where the transmissivity of the antenna was optimized for the task of entanglement distribution with TMST states of 5 GHz in an antenna of 3 cm. With an exponential profile of the impedance inside the antenna, reflectivity can be reduced down to $\sqrt{\eta} < 10^{-9}$, qualitatively matching the classical result of a horn antenna.

Using this description, we can obtain a reflectivity coefficient that depends on experimental parameters, such as the length of the antenna, the carrier frequency of quantum states, and the internal and external impedances, among others. This result is compatible with the description of the antenna as a distributed beam splitter, with its inputs being one of the modes of the TMST state together with a thermal state with N_{th} thermal photons coming from the environment. From the two output modes, the reflected one is discarded, whereas the transmitted one is sent to Bob. The main antenna aim is to minimize the reflections of Alice's input signal in order to preserve entanglement between the transmitted mode and the retained one.

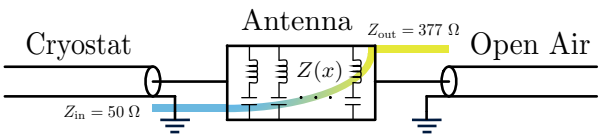

FIG. 3. Schematic representation of the circuit needed for a quantum communication protocol in which a quantum state is generated in a cryostat, and is then sent through an antenna into open air, where transmission is assumed to be focused. As is shown, a waveguide at impedance $Z_{\text{in}} = 50\ \Omega$ connects the cryostat with the antenna. The latter is a finite transmission line with variable impedance, $Z(x)$, designed to match the impedance of the cryostat with that of the open air, $Z_{\text{out}} = 377\ \Omega$, maximizing the transmissivity. The final waveguide represents the directed propagation of the signal in open air.

Backscattered thermal photons entering the emitting antenna might represent a certain problem for Alice and must be filtered. A straightforward, albeit somewhat challenging, solution for this problem is to use nonreciprocal microwave devices such as isolators (circulators) to protect entanglement-generating circuits from the unwanted thermal radiation.

Once the state has been successfully sent out of the cryostat, we have to address the effects of entanglement degradation in open air. Considering directed transmission in open air, we envision an infinite array of beam splitters to describe losses in open air, as represented in Fig. 4. Each one of these beam splitters will allow for the mixing of thermal noise with the state. Assuming constant temperature throughout the sequence of possible absorption events, meaning that the thermal noise in each of the beam splitters is characterized by N_{th}, we can obtain the reflectivity of an effective beam splitter based on an attenuation channel [80], which represents the decay of quantum correlations and amplitudes,

$$\eta_{\text{env}} = 1 - e^{-\mu L}. \tag{20}$$

Here, μ represents a density of reflectivity, which in turn models photon losses per unit length, and L is the traveled distance. This density of reflectivity can be interpreted as an attenuation coefficient that quantifies the specific attenuation of signals in a given environment. In this work we consider $\mu = 1.44 \times 10^{-6}\ \text{m}^{-1}$ for the specific attenuation of 5 GHz signals caused by the presence of oxygen molecules in the environment (see Refs. [91,92]).

We could go further and assume that, attached to the antenna (at constant temperature), there is another

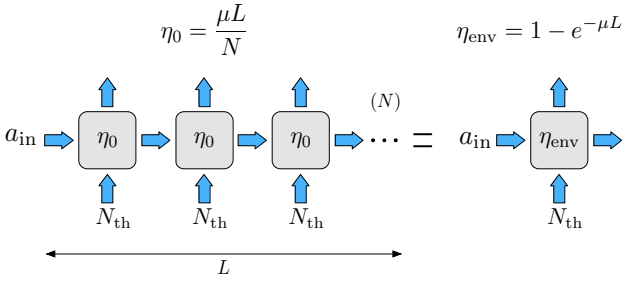

FIG. 4. Sketch of a beam splitter loss model of an open-air quantum channel. Entanglement degradation of a state propagating in open air at a constant temperature is modeled by an array of N beam splitters, each one introducing thermal noise characterized by N_{th} thermal photons, assuming constant temperature throughout the path. An infinite array of beam splitters ($N \to \infty$) can be approximated by a single beam splitter with reflectivity $\eta_{\text{env}} = 1 - e^{-\mu L}$, where L is the total channel length and μ is the reflectivity per unit length.

transmission line where the temperature is not constant throughout the trajectory, which leads to an inhomogeneous absorption probability. This is represented by the density of reflectivity $\mu(x)$, and the number of thermal photons $n(x)$. The latter still follows the Bose-Einstein distribution. An infinite array of beam splitters that reproduce these features (see Ref. [86]) can be replaced by a single beam splitter with an effective reflectivity and number of thermal photons given by

$$\eta_{\rm env} = 1 - e^{-\int_0^L \mathrm{d}x\mu(x)},$$
$$n_{\rm th} = \frac{\int_0^L \mathrm{d}x\mu(x)n(x)e^{-\int_x^L \mathrm{d}x'\mu(x')}}{1 - e^{-\int_0^L \mathrm{d}x\mu(x)}}, \tag{21}$$

where L represents the total length of the array. Given that we are extending the length in which the transmission line remains at cryogenic temperatures, we see that $n_{\rm th} \leq N_{\rm th}$.

Now that we have discussed how the signal is processed into the environment, let us characterize the resulting states. Assume that Alice generates a TMST state with n thermal photons, and sends one mode to Bob over a distance L through open air, with a thermal background characterized by $N_{\rm th}$ thermal photons. Then, the resulting state is what we call the "asymmetric" state

$$\Sigma_{\rm Asym} = (1+2n)\begin{pmatrix} \left[\left(\frac{1+2N_{\rm th}}{1+2n}\right)\eta_{\rm eff} + (1-\eta_{\rm eff})\cosh 2r\right]\mathbb{1}_2 & \sqrt{1-\eta_{\rm eff}}\sinh 2r\sigma_Z \\ \sqrt{1-\eta_{\rm eff}}\sinh 2r\sigma_Z & \cosh 2r\mathbb{1}_2 \end{pmatrix}, \tag{22}$$

where $\eta_{\rm eff} = 1 - e^{-\mu L}(1-\eta_{\rm ant})$ represents the combined reflectivities of the antenna $\eta_{\rm ant}$ and of the environment $\eta_{\rm env}$. A sketch of the layout that leads to this kind of state can be seen in Fig. 2(a). With this, using Eq. (5), we compute the partially transposed symplectic eigenvalue

$$\tilde{\nu}_-^{\rm out} = \tilde{\nu}_-^{\rm in} + \left(\frac{1}{2} + N_{\rm th}\right)\eta_{\rm ant} \tag{23}$$

for very low reflectivities, $\eta_{\rm ant}N_{\rm th} \ll 1$, with $\tilde{\nu}_{\rm in} = (1+2n)e^{-2r}$. Note that, by reducing the reflectivity of the antenna, the impact of thermal noise is reduced, and the partially transposed symplectic eigenvalue approaches that of the input state. In this extreme case, entanglement is fully preserved.

Let us use the partially transposed symplectic eigenvalue to compute the limit of entanglement. We use the negativity as a measure of Gaussian entanglement, $\mathcal{N} = \max\{0, (1-\tilde{\nu}_-)/2\tilde{\nu}_-\}$, such that this limit occurs for $\tilde{\nu}_- = 1$. This constitutes a bound on the reflectivity; all smaller values of $\eta_{\rm eff}$ will result in entanglement preservation. This result is

$$\eta_{\rm max} = \frac{1}{1 + \dfrac{N_{\rm th}}{1 + \dfrac{2n(1+n)}{1-(1+2n)\cosh(2r)}}}, \tag{24}$$

together with the conditions $n < e^{-r}\sinh(r)$ and $r > 0$. With this bound, the maximum distance entanglement can survive is

$$L_{\rm max} = -\frac{1}{\mu}\log(1-\eta_{\rm max}). \tag{25}$$

Imagine that TMST states are generated in the cryostat at 50 mK temperature, with thermal photons $n \sim 10^{-2}$, and squeezing $r = 1$. In open air, at 300 K, the number of thermal photons is $N_{\rm th} \sim 1250$. Assuming a perfect antenna ($\eta_{\rm ant} = 0$), the maximum distance the state can travel before entanglement completely degrades is $L_{\rm max} \sim 550\,\mathrm{m}$.

As a different approach to the entangled resource, we assume that a TMST state is generated at an intermediate spot between both parties, and that each mode is sent through an antenna and travels some distance L_i with $i = \{1,2\}$ before reaching Alice and Bob. Then, each mode will see an effective reflectivity of $\eta_{\rm eff}^{(i)} = 1 - e^{-\mu L_i}(1-\eta_{\rm ant})$, combining the effects of the antenna and the environment. We assume for simplicity that $L_1 + L_2 = L$, where L is the linear distance between Alice and Bob. The covariance matrix of such a state, which we refer to as "symmetric," is

$$\Sigma_{\rm Sym} = (1+2n)\begin{pmatrix} \left[\left(\frac{1+2N_{\rm th}}{1+2n}\right)\eta_{\rm eff}^{(1)} + (1-\eta_{\rm eff}^{(1)})\cosh 2r\right]\mathbb{1}_2 & \sqrt{(1-\eta_{\rm eff}^{(1)})(1-\eta_{\rm eff}^{(2)})}\sinh 2r\sigma_Z \\ \sqrt{(1-\eta_{\rm eff}^{(1)})(1-\eta_{\rm eff}^{(2)})}\sinh 2r\sigma_Z & \left[\left(\frac{1+2N_{\rm th}}{1+2n}\right)\eta_{\rm eff}^{(2)} + (1-\eta_{\rm eff}^{(2)})\cosh 2r\right]\mathbb{1}_2 \end{pmatrix}, \tag{26}$$

and corresponds to the layout represented in Fig. 2(b). With this state, the maximum distance entanglement can survive is $L_{\max} \sim 480$ m.

Throughout this manuscript, we refer to these states as the (asymmetric and/or symmetric) lossy TMST states, the bare states, or the TMST states distributed through open air.

Furthermore, we could also consider the specific attenuation caused by the presence of water vapor in the environment [91]. This would lead to higher attenuation coefficients, thus reducing the distances that entanglement can survive. For an average water vapor density, these distances are 450 and 390 m for asymmetric and symmetric states, respectively. They become 400 m for asymmetric states and 350 m for symmetric states in a maximum water vapor density scenario.

C. Overcoming entanglement degradation: distillation and swapping with microwaves

We have seen that entanglement distribution between two parties is limited by environmental noise, as well as by photon losses. Considering we have a perfect antenna, these factors can limit the maximum distance entanglement can survive to a few hundred meters. Since an amplification protocol only contributes to the degradation of quantum correlations (see Appendix A), we investigate entanglement distillation and entanglement swapping, two techniques that could improve both the reach and the quality of entanglement, at the expense of efficiency [70].

1. Entanglement distillation

This technique aims at increasing entanglement in quantum states by means of local operations. Let us briefly review different ways to distill entanglement. One of them is noiseless linear amplification, a nondeterministic operation [93,94] that requires nonincreasing distinguishability of amplified states, and which has recently been achieved in the microwave regime [71]. It also requires efficient photocounting, which is where the nondeterministic part comes into play. At the core of this protocol lies a process based on the quantum scissors [95]. The gain of this procedure is inversely proportional to the success probability, which also decreases as the number of resources increases, making it very costly.

Another widely known protocol is Gaussian distillation, which is also nondeterministic, but it requires only two initial copies of a state, as well as efficient photodetection. If the incoming entangled state is Gaussian then it is initially de-Gaussified by combining two copies of said state with balanced beam splitters and keeping the transmitted state when any number of photons has been detected at the reflected modes [96]. Another possible de-Gaussification protocol applies an operation $\hat{Z} = (1-\omega)a^\dagger a + \omega a a^\dagger$ [97] on a quantum state without requiring a copy. Gaussian distillation begins when two copies of the resulting state are mixed by 50:50 beam splitters and, if no photons are reflected, the operation is applied again [96,98]. Provided that the initial states were entangled, this process leads to a non-Gaussian state with higher entanglement. However, it is also costly in terms of the number of resources, and it only produces a state that is Gaussian (and with higher entanglement) in an infinite-application limit of the Gaussification channel.

Finally, we review another nondeterministic protocol, which does not require the storage or production of simultaneous copies of a quantum state, and whose gain is also inversely proportional to the success probability. This protocol is called probabilistic photon subtraction [99], and it utilizes non-Gaussian operations in order to distill entanglement, as we have seen in the previous protocols. However, in this situation, we do not look to re-Gaussify the state afterwards. A discussion about the heuristic photon-subtraction protocol with TMSV states, the more theoretical approach that does not consider the effects of beam splitters and measurement, can be found in Appendix B.

Probabilistic photon subtraction starts with an entangled state, for example a TMSV state. This can be produced by two single-mode squeezed states with squeezing parameter r, which are combined by a 50:50 beam splitter, as shown in Fig. 5, resulting in a TMSV state,

$$\sqrt{1-\lambda^2}\sum_{n=0}^{\infty}\lambda^n|n,n\rangle_{AB} \tag{27}$$

with $\lambda = \tanh(r)$. The next step of the protocol is to mix each mode with an ancillary vacuum state at two highly

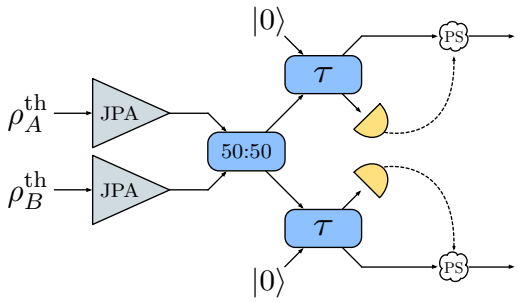

FIG. 5. Sketch of a photon-subtraction scheme applied to two-mode squeezed thermal states, which are generated from single-mode squeezed thermal states by JPAs, subsequently combined in a balanced beam splitter. Each mode of the resulting state is then combined with an ancillary vacuum state in high-transmissivity (we consider $\tau = 0.95$) beam splitters, with photocounters placed at each reflected path. The resulting state shows higher entanglement for low values of the squeezing parameter, where the limit for enhancement will vary depending on the number of photons detected.

transmitting, identical beam splitters. The output photon-subtracted state is postselected depending on the outcome of the photocounts performed at each beam splitter. Here, we focus on photon-subtracted TMSV states where the same number of photons is subtracted from each mode. The resulting $2k$-photon-subtracted TMSV state is then

$$|\psi^{(2k)}\rangle_{AB} = P_{2k}^{-1/2} \sum_{n=0}^{\infty} a_n^{(k)} |n,n\rangle_{AB} \tag{28}$$

with $a_n^{(k)} \equiv \sqrt{1-\lambda^2}\lambda^{n+k}\binom{n+k}{k}(1-\tau)^k\tau^n$ and $P_{2k} \equiv \sum_{n=0}^{\infty} |a_n^{(k)}|^2$, which can be interpreted as the probability of successfully subtracting k photons from each mode of a TMSV state. The sum converges to $P_{2k} = (1-\lambda^2)(\lambda - \lambda_\tau)^{2k}\, {}_2F_1(k+1,k+1;1;\lambda_\tau^2)$, where ${}_2F_1(a,b;c;z)$ is the Gaussian hypergeometric function and $\lambda_\tau \equiv \tau\lambda$. In what follows, we focus on the cases $k = 1, 2$, which correspond to two-photon subtraction (2PS) and four-photon subtraction (4PS), respectively, and whose corresponding success probabilities are

$$\begin{aligned} P_2 &= (1-\lambda^2)\lambda^2(1-\tau)^2\frac{(1+\lambda_\tau^2)}{(1-\lambda_\tau^2)^3}, \\ P_4 &= 4(1-\lambda^2)\lambda^4(1-\tau)^4\frac{(1+\lambda_\tau^4+4\lambda_\tau^2)}{(1-\lambda_\tau^2)^5}. \end{aligned} \tag{29}$$

If photon subtraction is successful for any (nonzero) number of photons, the resulting state shows increased entanglement with respect to the TMSV state in a certain interval. This can be seen by computing the negativity $\mathcal{N}(\rho^{(2k)})$ of the family of states (28). We find that, for $\rho^{(2k)} \equiv |\psi^{(2k)}\rangle\langle\psi^{(2k)}|$, the negativity is

$$\mathcal{N}(\rho^{(2k)}) = \frac{A_k - 1}{2}, \tag{30}$$

where

$$A_k \equiv \frac{(\sum_{n=0}^{\infty} a_n^{(k)})^2}{P_{2k}}. \tag{31}$$

Performing the sum we obtain

$$\mathcal{N}(\rho^{(2k)}) = \frac{1}{2}\left(\frac{(1-\lambda_\tau)^{-2(k+1)}}{{}_2F_1(k+1,k+1;1;\lambda_\tau^2)} - 1\right), \tag{32}$$

which describes the negativity of the heuristic photon-subtraction protocol (see Appendix B) in the limit $\tau \to 1$, while reproducing the negativity of the TMSV state, $\mathcal{N}_{\mathrm{TMSV}} = \lambda/(1-\lambda)$, in the case $\tau \to 1$ and $k = 0$.

In Fig. 6(a) we represent negativity differences as a function of the initial squeezing r. We subtract the negativity of the TMSV state from those resulting from two-photon (blue) and four-photon (red), heuristic (solid) and probabilistic (dashed), subtraction with a beam splitter transmissivity $\tau = 0.95$. Note that probabilistic photon subtraction works for lower squeezing, while heuristic photon subtraction is always advantageous. In Fig. 6(b), we display the success probability of two-photon (blue dashed line) and four-photon (red dashed line) subtraction. Observe that 2PS shows higher probability than 4PS, whereas the latter shows higher improvement than the former. As the squeezing parameter increases, both probabilities grow closer, as probabilistic PS loses its advantage.

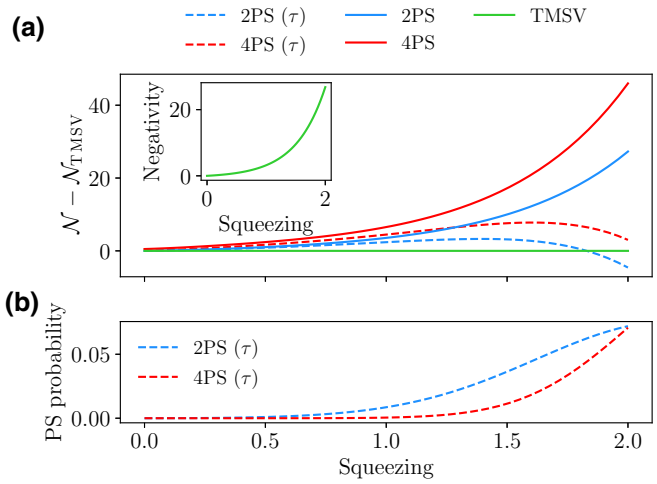

FIG. 6. (a) Negativity difference between photon-subtracted and bare TMSV states, represented against the initial squeezing parameter. The blue and red curves represent two- and four-photon subtraction, respectively, whereas the green curve represents the no-gain line, above which any point represents an improvement in negativity. Curves associated with probabilistic photon subtraction appear dashed, whereas the solid curves are associated with heuristic photon subtraction. We have considered the transmissivity of the beam splitters involved in probabilistic photon subtraction to be $\tau = 0.95$. In the inset, we represent the negativity curve for the TMSV state versus the initial squeezing parameter. (b) Success probability of symmetric photon-subtraction schemes: two-photon subtraction (2PS) is represented with a blue dashed line, and four-photon subtraction (4PS) is represented with a red dashed line.

The rate of two-mode squeezed state generation is defined by the effective bandwidth of JPAs. In the case of conventional resonator-based JPAs, these bandwidths are typically of the order of about 10 MHz [88]. By exploiting more advanced designs based on traveling-wave Josephson parametric amplifiers, one can hope to increase these bandwidth to about 1 GHz. However, the price for this increase is typically lower squeezing levels and higher noise photon numbers.

When dealing with our lossy TMST states, we consider a two-photon-subtraction protocol that is applied right before the teleportation experiment, in order to prepare the entangled resource for enhanced performance.

This means that we apply photon subtraction on states that have already traveled through open air. In the case of TMSV states, photon subtraction is beneficial for low squeezing, which translates into low entanglement. In the case of lossy TMST states, entanglement is affected by the initial squeezing, but also by the distance, since reducing it means reducing photon loses and the presence of thermal noise in the state. Consequently, better performance of the teleportation protocol using photon-subtracted entangled states as the resource occurs for small distances. The submatrices of the covariance matrix that characterizes the entangled resource, written as $\Sigma_A = \alpha \mathbb{1}_2$, $\Sigma_B = \beta \mathbb{1}_2$, and $\varepsilon_{AB} = \gamma \sigma_z$, are modified by a symmetric two-photon-subtraction process as

$$\tilde{\Sigma}_A = \left[1 - 2\tau \frac{(1-\alpha)(1+\beta) + \gamma^2 + ((1-\alpha)(1-\beta) - \gamma^2)\tau}{(1+\alpha)(1+\beta) - \gamma^2 + 2(1-\alpha\beta+\gamma^2)\tau + ((1-\alpha)(1-\beta) - \gamma^2)\tau^2}\right]\mathbb{1}_2, \tag{33a}$$

$$\tilde{\Sigma}_B = \left[1 - 2\tau \frac{(1+\alpha)(1-\beta) + \gamma^2 + ((1-\alpha)(1-\beta) - \gamma^2)\tau}{(1+\alpha)(1+\beta) - \gamma^2 + 2(1-\alpha\beta+\gamma^2)\tau + ((1-\alpha)(1-\beta) - \gamma^2)\tau^2}\right]\mathbb{1}_2, \tag{33b}$$

$$\tilde{\varepsilon}_{AB} = \frac{4\tau\gamma}{(1+\alpha)(1+\beta) - \gamma^2 + 2(1-\alpha\beta+\gamma^2)\tau + ((1-\alpha)(1-\beta) - \gamma^2)\tau^2}\sigma_z, \tag{33c}$$

whose success probability is given by

$$P = 4(1-\tau)^2 \frac{[1 - \alpha\beta + \gamma^2 + ((1-\alpha)(1-\beta) - \gamma^2)\tau]^2 - (\alpha-\beta)^2 + 4\gamma^2}{[(1+\alpha)(1+\beta) - \gamma^2 + 2(1-\alpha\beta+\gamma^2)\tau + ((1-\alpha)(1-\beta) - \gamma^2)\tau^2]^3}. \tag{34}$$

See Appendix C for the general expressions. In order for these submatrices to characterize a covariance matrix, they need to satisfy a positivity condition, as well as the uncertainty principle. Both these requirements can be summarized as

$$|\sqrt{\det\tilde{\Sigma}} - 1| \geq |\tilde{\alpha} - \tilde{\beta}|, \tag{35}$$

given that we have used $\tilde{\Sigma}_A = \tilde{\alpha}\mathbb{1}_2$, $\tilde{\Sigma}_B = \tilde{\beta}\mathbb{1}_2$. Unfortunately, the state resulting from photon subtraction is not Gaussian, and thus it is not completely characterized by the covariance matrix. In this case, we use the characteristic function to describe the photon-subtracted TMST states. The general expression for the characteristic function of a probabilistically two-photon-subtracted Gaussian state (where one photon has been subtracted in each mode) can be found in Appendix C. Furthermore, see Appendix B for an equivalent discussion regarding heuristic photon subtraction.

2. Entanglement swapping

In this section we contemplate the CV version of entanglement swapping [100], a procedure that can be used to reduce the distance that states have to travel through the environment, and hence attenuate the effects of entanglement degradation. We consider the case in which we have two entangled states, shared by three parties pairwisely. That is, between Alice and Charlie, and between Charlie and Bob. Entanglement swapping is a technique that allows for the conversion of two bipartite entangled states into a single one shared by initially unconnected parties. By performing measurements in a maximally entangled basis, Charlie is able to transform the entangled resources he shares with Alice and with Bob into a single entangled state shared only by Alice and Bob. In the CV formalism, these measurements are described by Homodyne detection, and their effect on the state is computed as we have seen in the CV teleportation protocol. Consider that these states are Gaussian, with covariance matrices

$$\Sigma_1 = \begin{pmatrix} \Sigma_A & \varepsilon_{AB} \\ \varepsilon_{AB}^\intercal & \Sigma_B \end{pmatrix}, \qquad \Sigma_2 = \begin{pmatrix} \Sigma_C & \varepsilon_{CD} \\ \varepsilon_{CD}^\intercal & \Sigma_D \end{pmatrix}, \tag{36}$$

and null displacement vectors. Then, the covariance matrix of the remaining state,

$$\Sigma^{\mathrm{ES}} = \begin{pmatrix} \tilde{\Sigma}_A & \tilde{\varepsilon}_{AD} \\ \tilde{\varepsilon}_{AD}^\intercal & \tilde{\Sigma}_D \end{pmatrix}, \tag{37}$$

conditioned by the measurement results is characterized by

$$\tilde{\Sigma}_A = \Sigma_A - \frac{\varepsilon_{AB}(\Sigma_B + \sigma_z\Sigma_C\sigma_z)\varepsilon_{AB}^\intercal}{\det(\Sigma_B + \sigma_z\Sigma_C\sigma_z)}, \tag{38a}$$

$$\tilde{\Sigma}_D = \Sigma_D - \frac{\varepsilon_{CD}(\Sigma_C + \sigma_z\Sigma_B\sigma_z)\varepsilon_{CD}^\intercal}{\det(\Sigma_B + \sigma_z\Sigma_C\sigma_z)}, \tag{38b}$$

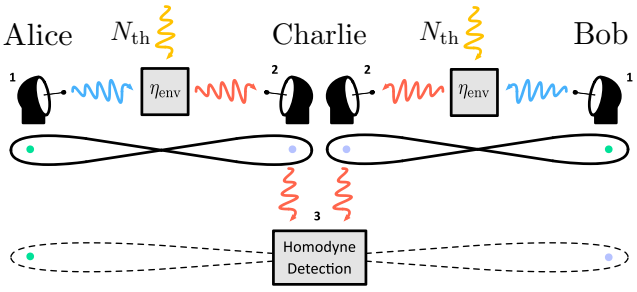

FIG. 7. Sketch of the optimal entanglement swapping scheme involving three parties and three key steps. First, Alice and Bob generate two-mode squeezed thermal states and, while keeping one of the modes each, send the others through open air, where they are subject to photon loss and get mixed with thermal noise. Second, Charlie receives and processes both modes, and third, he uses them to perform Homodyne detection. In the end, Charlie is able to transform the pairwisely entangled states he shares with Alice and with Bob independently into an entangled state held solely between Alice and Bob.

$$\tilde{\varepsilon}_{AD} = \frac{\varepsilon_{AB}(\Sigma_B\sigma_z + \sigma_z\Sigma_C)\varepsilon_{CD}^{\intercal}}{\det(\Sigma_B + \sigma_z\Sigma_C\sigma_z)}. \tag{38c}$$

We observe that, in the setup we are considering, the only protocol that presents an improvement in negativity with respect to the bare states is that in which Alice and Bob generate the two-mode entangled states, and each send one of the modes to Charlie. This setup is represented in Fig. 7. Then, the two modes used for entanglement swapping are those that have become mixed with environmental noise. Nevertheless, this enhancement occurs for large distances, which implies low negativities, and works significantly better in low-temperature environments, where $N_{\rm th}$ is reduced. Considering $\Sigma_A = \Sigma_D = \alpha\mathbb{1}_2$, $\Sigma_B = \Sigma_C = \beta\mathbb{1}_2$, and $\varepsilon_{AB} = \varepsilon_{CD} = \gamma\sigma_z$, then we can characterize the covariance matrix of the resulting resource by

$$\tilde{\Sigma}_A = \left(\alpha - \frac{\gamma^2}{2\beta}\right)\mathbb{1}_2, \tag{39a}$$

$$\tilde{\Sigma}_D = \left(\alpha - \frac{\gamma^2}{2\beta}\right)\mathbb{1}_2, \tag{39b}$$

$$\tilde{\varepsilon}_{AD} = \frac{\gamma^2}{2\beta}\sigma_z. \tag{39c}$$

The condition for this characterization to be appropriate is given by

$$\left|\sqrt{\det\Sigma_1} - \frac{\beta}{\alpha}\right| \geq 0. \tag{40}$$

See Appendix D for further discussion.

IV. EXPERIMENTAL LIMITATIONS TO PHOTOCOUNTING AND HOMODYNING WITH MICROWAVES

In this section, we review current advances on photocounting and homodyne detection techniques with microwave quantum technologies. These techniques are vital for photon subtraction, as well as for entanglement swapping and quantum teleportation, which are the processes described in this manuscript.

A. Photodetection

Traditionally, the problem of detecting microwaves has been the low energy of the signals when compared to the optical regime. Any of the entanglement distillation protocols we have discussed will require some kind of photodetection scheme. In particular, for photon subtraction, a photocounter for microwave photons is required. In the current landscape of microwave quantum technologies, there have been recent proposals for nondemolition detection of itinerant single microwave photons [101–103] in circuit-QED setups, with detection efficiencies ranging from 58% to 84%. Based on similar setups, a photocounter has been proposed [71] that can detect up to three microwave photons.

This device is able to catch an incoming wavepacket in a buffer resonator, which is then transferred into the memory by means of pumping a Josephson ring modulator. Then, the information about the number of photons in the memory is transferred to a transmon qubit, which is coupled to the memory modes, and from there, it is read bit by bit. Consequently, this photocounter requires previous knowledge on the waveform and the arrival time of the incoming mode to be detected. Furthermore, this device is not characterized by a single quantum efficiency; rather, the detection efficiency varies depending on the number of photons. That is, 99% for zero photons, 76% ± 3% for a single photon, 71% ± 3% for two photons, and 54% ± 2% for three photons, assuming a dark count probability of 3% ± 0.2% and a dead time of 4.5 μs.

B. Homodyne detection

Homodyne detection allows one to extract information about a single quadrature. It can be used to perform CV-Bell measurements, i.e., a projective measurement in a maximally-quadrature-entangled basis for CV states. One way to perform Bell measurements with propagating CV states is to use the analog feedforward technique, as demonstrated in Ref. [10]. This approach requires operating two additional phase-sensitive amplifiers in combination with two hybrid rings and a directional coupler, which effectively implements a projection operation for conjugate quadratures of propagating electromagnetic fields. An alternative, more conventional approach can be implemented by adapting microwave single-photon detectors to the well-known optics homodyning techniques.

As we have seen, entanglement swapping provides an advantage if this measurement scheme is used without averaging over the results (single-shot homodyning), whereas the Braunstein-Kimble quantum teleportation protocol assumes that this average is performed, given an unknown coherent state. In theory, single-shot homodyning can be implemented by using quantum-limited superconducting amplifiers and standard demodulation techniques [104]. However, some fundamental aspects of the "projectiveness" of this operation and its importance for the Bell detection measurements or for photon subtraction are still unclear and must be verified.

See Appendix E for more involved descriptions of errors associated with these measurement techniques.

V. OPEN-AIR MICROWAVE QUANTUM TELEPORTATION FIDELITIES

In this section, we compute the average teleportation fidelity for different resource states. In all cases, the teleported state is a coherent state $|\alpha_0\rangle\langle\alpha_0|$.

A. Two-mode squeezed vacuum resource

The case of a TMSV state is particularly simple, as we can simply plug its covariance matrix into Eq. (17),

$$\overline{F}_{\mathrm{TMSV}} = \frac{1+\lambda}{2}. \tag{41}$$

When symmetric $2k$-photon subtraction is performed, the formula for Gaussian average fidelity can no longer be invoked. The results for $k = 1, 2$ (2PS and 4PS, respectively) are

$$\overline{F}_{\mathrm{2PS}} = \left(1 - \lambda_\tau + \frac{\lambda_\tau^2}{2}\right)\frac{(1+\lambda_\tau)^3}{2(1+\lambda_\tau^2)},$$
$$\overline{F}_{\mathrm{4PS}} = \frac{(1+\lambda_\tau)^5[8-\lambda_\tau(2-\lambda_\tau)(8-3\lambda_\tau(2-\lambda_\tau))]}{16(1+4\lambda_\tau^2+\lambda_\tau^4)}, \tag{42}$$

with $\lambda_\tau = \lambda\tau$.

In Fig. 8, we represent the result of subtracting the fidelity associated with the bare TMSV state to those associated with two-photon-subtracted (2PS, blue) and four-photon-subtracted (4PS, red) TMSV states. Fidelity differences associated with heuristic photon subtraction appear as solid lines, whereas those associated with probabilistic photon subtraction appear dashed. The green solid line represents the no-gain line, above which any photon-subtracted state presents an advantage in fidelity. Note that photon subtraction works better for low squeezing, and as we increase it, we see that using the TMSV state as a resource for teleportation renders a higher fidelity than probabilistic photon subtraction, while heuristic photon subtraction tends to the TMSV result.

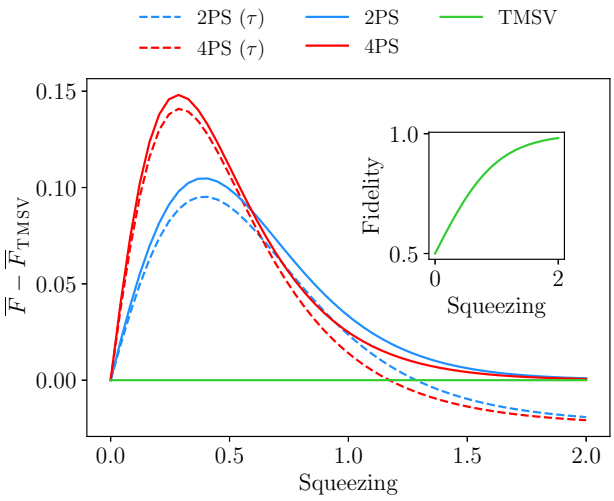

FIG. 8. Average fidelity of CV quantum teleportation of an unknown coherent state with respect to the initial squeezing parameter. We subtract the average fidelity associated with a TMSV state resource from the average fidelities of two-photon-subtracted (2PS, blue) and four-photon-subtracted (4PS, red) TMSV states. Curves associated with probabilistic photon subtraction appear dashed, whereas the solid curves are associated with heuristic photon subtraction. The green curve describes the TMSV case, which delimits the no-gain line, above which any point represents an improvement in fidelity due to photon subtraction. In the inset, we plot the average fidelity associated with a TMSV state against the initial squeezing parameter. We have considered the transmissivity of the beam splitters involved in probabilistic photon subtraction to be $\tau = 0.95$.

B. Two-mode squeezed thermal resource

We now study the teleportation fidelity associated with a two-mode squeezed thermal state, sent through a lossy and noisy channel defined by the combination of the antenna and an environment with N_{th} photons. By defining $\Sigma_A = \alpha\mathbb{1}_2$, $\Sigma_B = \beta\mathbb{1}_2$, and $\varepsilon_{AB} = \gamma\sigma_z$, we can write the average fidelity as

$$\overline{F}_{\mathrm{TMST}} = \frac{1}{1+(\alpha+\beta-2\gamma)/2}. \tag{43}$$

If we consider the composition of k teleportation protocols where each of the parties involved is separated by L/k, with L the total distance aimed to cover. The final average fidelity is then given by

$$\overline{F}^{(k)}_{\mathrm{TMST}} = \frac{1}{1+(k-1/2)(\alpha+\beta-2\gamma)}, \tag{44}$$

such that $\overline{F}_{\mathrm{TMST}} > \overline{F}^{(k)}_{\mathrm{TMST}}$ for $k > 1$. Since the composition of teleportation protocols does not improve the overall fidelity, we study entanglement distillation and entanglement swapping in search for such gain. However, this fidelity composition may improve the overall fidelity when

TABLE I. Parameters for a terrestrial (1 atm of pressure, temperature of 300 K) two-mode squeezed thermal state generated at a 50 mK cryostat, for a frequency of 5 GHz. These parameter values correspond to an Earth-based quantum teleportation scenario.

Parameter	Symbol	Value
Losses per unit of length	μ	1.44×10^{-6} m^{-1}
Atmospheric temperature	T	300 K
Mean photon number	N_{th}	1250
Squeezing parameter	r	1
Thermal photon number (signal)	n	10^{-2}
Transmission coefficient	τ	0.95
Antenna reflectivity	η_{ant}	0

diffraction effects at the termination of the antenna come into play, which will reduce the reach of entanglement from the hundreds to the tens of meters.

In Table I we present the parameters we use to represent the different fidelity curves in this section.

1. Asymmetric case

Assume that Alice generates a TMST state and sends one of the modes to Bob. Then, the covariance matrix of the state, given in Eq. (22), is characterized by

$$\alpha = (1+2N_{\text{th}})\eta_{\text{eff}} + (1+2n)(1-\eta_{\text{eff}})\cosh 2r, \quad (45a)$$

$$\beta = (1+2n)\cosh 2r, \quad (45b)$$

$$\gamma = (1+2n)\sqrt{1-\eta_{\text{eff}}}\sinh 2r, \quad (45c)$$

which results in an average fidelity

$$\overline{F}_{\text{TMST}} = \left[1 + \left(\frac{1}{2}+N_{\text{th}}\right)\eta_{\text{eff}} + \left(\frac{1}{2}+n\right)(2-\eta_{\text{eff}})\cosh 2r - (1+2n)\sqrt{1-\eta_{\text{eff}}}\sinh 2r\right]^{-1} \quad (46)$$

with $\eta_{\text{eff}} = 1 - e^{-\mu L}(1-\eta_{\text{ant}})$.

2. Symmetric case

In this case, we consider that the resource state is generated at an intermediate point between Alice and Bob, and is sent to both of them, such that now both modes are affected by the lossy and noisy channel described above. The covariance matrix of this state, presented in Eq. (26), is characterized by

$$\alpha = (1+2N_{\text{th}})\eta_{\text{eff}} + (1+2n)(1-\eta_{\text{eff}})\cosh 2r, \quad (47a)$$

$$\beta = (1+2N_{\text{th}})\eta_{\text{eff}} + (1+2n)(1-\eta_{\text{eff}})\cosh 2r, \quad (47b)$$

$$\gamma = (1+2n)(1-\eta_{\text{eff}})\sinh 2r, \quad (47c)$$

where we have assumed that $L_1 = L_2 = L/2$, and thus $\eta_{\text{eff}}^{(1)} = \eta_{\text{eff}}^{(2)} = \eta_{\text{eff}} = 1 - e^{-\mu L/2}(1-\eta_{\text{ant}})$. Then, the average fidelity can be written as

$$\overline{F}_{\text{TMST}} = [1 + (1+2N_{\text{th}})\eta_{\text{eff}} + (1+2n)(1-\eta_{\text{eff}})\cosh 2r - (1+2n)(1-\eta_{\text{eff}})\sinh 2r]^{-1}. \quad (48)$$

Note that, for short distances, the fidelities associated with the asymmetric and symmetric states coincide. That is, at first order in $\mu L \ll 1$, and with $\eta_{\text{ant}} = 0$,

$$\overline{F}_{\text{TMST}} \approx \left[1 + (1+2N_{\text{th}})\frac{\mu L}{2} + (1+2n)\left(1-\frac{\mu L}{2}\right)e^{-2r}\right]^{-1}. \quad (49)$$

When considering a lossy antenna, we observe higher entanglement degradation in the symmetric state due to the fact that both modes of the state are output by an antenna, whereas only one mode of the asymmetric state goes through it. Although $\sqrt{\eta_{\text{ant}}}$ can theoretically be reduced below 10^{-9} [86], this leads to a slightly lower fidelity in the case of the symmetric state. In the figures appearing in this section, however, we consider $\eta_{\text{ant}} = 0$ for simplicity.

C. Fidelity with photon subtraction

If we consider a symmetric two-photon-subtraction process, in which the desired resource has lost a single photon in each mode, the average fidelity becomes

$$\overline{F}_{\text{2PS}} = \frac{1}{4}\left[1 + \tau\frac{-\alpha\beta + (1+\gamma)^2 + ((1-\alpha)(1-\beta)-\gamma^2)\tau}{(1+\alpha)(1+\beta)-\gamma^2-(\alpha\beta-(1-\gamma)^2)\tau}\right]^3 \times \left[1 + \frac{(1-\alpha\beta+\gamma^2)^2 - (\alpha-\beta)^2 + 4\gamma^2 + 4\gamma((1-\alpha)(1-\beta)-\gamma^2)\tau}{(1-\alpha\beta+\gamma^2+((1-\alpha)(1-\beta)-\gamma^2)\tau)^2 - (\alpha-\beta)^2 + 4\gamma^2}\right]. \quad (50)$$

In Fig. 9 we represent the difference in fidelities associated with a CV open-air quantum teleportation protocols for an unknown coherent state, using two-mode squeezed thermal states distributed through open air as a resource, against the traveled distance. We subtract the fidelity associated with the bare resource (TMST) from those related to two-photon-subtracted symmetric (blue) and asymmetric (red) states, as well as entanglement-swapped (orange) states. We consider both heuristic (solid lines) and probabilistic (dashed lines, labeled τ) photon subtraction. In Fig. 10(a), we can see the fidelity associated with the bare resource, knowing that it coincides for the symmetric and asymmetric states in the region $\mu L \ll 1$. The solid green line represents the no-gain line, above which any point represents an improvement in fidelity over the bare state. The former gives an enhancement for short distances, whereas the latter helps extend the point where the classical limit is reached. One of the reasons the gain related to photon subtraction is lost might be the increase of thermal photons in the state, which occurs for increasing L. This happens because, as photon losses are more relevant, the cost of doing photon subtraction is higher: if we subtract thermal photons, the entanglement hardly increases, whereas if we subtract photons from the signal, entanglement decreases. Using a pale red background, we represent the region in which the fidelity associated with the bare resource reaches the maximum classical value of $1/2$.

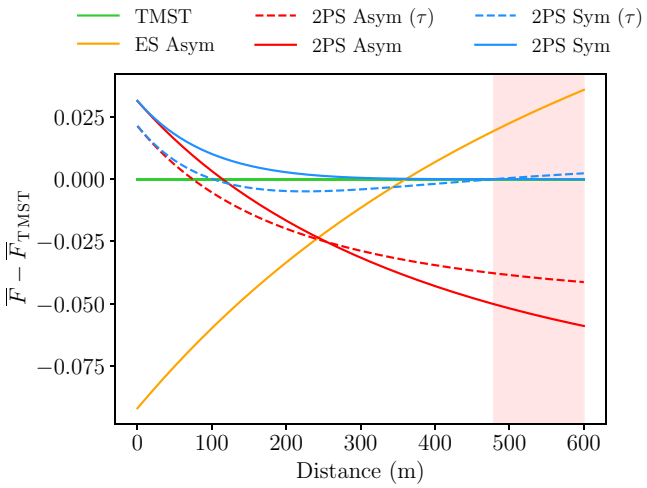

FIG. 9. Average fidelity of CV quantum teleportation of an unknown coherent state using an entangled resource distributed through open air, represented versus the traveled distance. We subtract the average fidelity associated with the TMST state distributed through open air (green) from the average fidelities of the two-photon-subtracted asymmetric (2PS asym) and symmetric (2PS sym) states, represented in red and blue, respectively, as well as from the average fidelity of the entanglement-swapped asymmetric (ES asym) state, in orange. We represent the states resulting from probabilistic photon subtraction (dashed), as well as heuristic photon subtraction (solid). The pale red background represents the region where the fidelity is below the maximum classical fidelity of $1/2$, and the quantum advantage is lost. The green line then shows no gain, and any point above it corresponds to an improvement in fidelity. Parameters are $n = 10^{-2}$, $N_{\mathrm{th}} = 1250$, $r = 1$, $\mu = 1.44 \times 10^{-6}\ \mathrm{m}^{-1}$, $\eta_{\mathrm{ant}} = 0$, $\tau = 0.95$.

In Fig. 10, we represent various features of the two-mode squeezed thermal states distributed through open air: (a) average fidelity, which coincides for the symmetric and asymmetric states for $\mu L \ll 1$; (b) logarithmic negativity $E_{\mathcal{N}} = \log_2(2\mathcal{N} + 1)$ of the symmetric (green) and asymmetric (purple) states; (c) success probability of photon subtraction [see Eq. (34)] for symmetric (blue, dashed) and asymmetric (red, dashed) states, against $(\overline{F}_{\mathrm{2PS}} - \overline{F}_{\mathrm{TMST}})/(1 - \overline{F}_{\mathrm{TMST}})$, which represents the gain in fidelity of the photon-subtraction schemes, weighted to show larger values when the gain occurs at larger fidelities; (d) efficiency of photon subtraction at $x = 0$, computed as $P(\overline{F}_{\mathrm{2PS}} - \overline{F}_{\mathrm{TMST}})$, against different values of the transmissivity, with $\tau \in [0.9, 1]$. Note that greater fidelity gains come at lower success probabilities for photon subtraction, which can be reflected in the efficiency (of the order of 10^{-4}). The latter achieves maximum values for a transmissivity of $\tau \approx 0.92$, and goes to zero with the probability, as τ goes to 1.

In an attempt to explain the crossing that occurs between the probabilistically-photon-subtracted and bare fidelities, which delimits the region in which photon subtraction results in an enhanced teleportation fidelity, we consider the following approach: we attempt to find the Gaussian state that is related to our non-Gaussian photon-subtracted state by the same teleportation fidelity. Essentially, we are looking to identify the photon-subtracted states with Gaussian resources in order to compute the negativities from their covariance matrices, and investigate what happens to entanglement at the points where fidelity with photon-subtracted states loses its advantage. A similar approach can be found in Appendix B for heuristic photon subtraction. First, know that the fidelity with two-photon subtraction can be written as

$$\overline{F}_{\mathrm{2PS}} = \frac{1+g}{\sqrt{\det[\mathbb{1}_2 + \tilde{\Gamma}/2]}}, \tag{51}$$

where $\tilde{\Gamma} \equiv \sigma_Z \tilde{\Sigma}_A \sigma_Z + \tilde{\Sigma}_B - \sigma_Z \tilde{\varepsilon}_{AB} - \tilde{\varepsilon}_{AB}^{\intercal} \sigma_Z$, and $\tilde{\Sigma}_A$, $\tilde{\Sigma}_B$, and $\tilde{\varepsilon}_{AB}$ are defined in Eq. (33). Here, g is the result of integrating all the non-Gaussian corrections to the characteristic function, which enforces the non-Gaussianity of the state resulting from photon subtraction (see Appendix C for the general expression). We split the terms in the previous equation and write

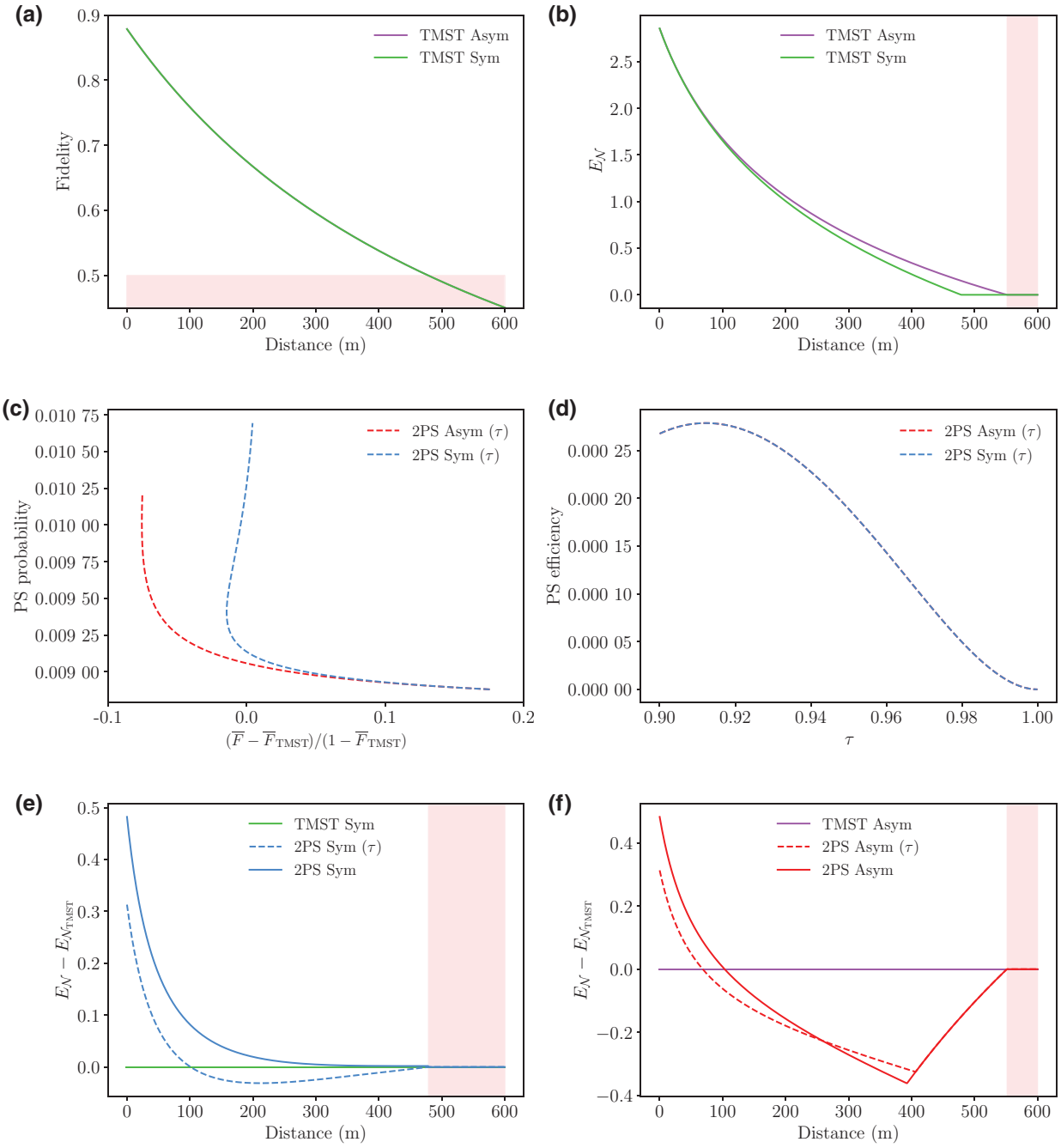

FIG. 10. Various features of the symmetric and asymmetric TMST states distributed through open air. (a) Average fidelity of the CV quantum teleportation protocol of an unknown coherent state using either symmetric or asymmetric lossy TMST states, represented against the traveled distance. (b) Logarithmic negativities $E_{\mathcal{N}} = \log_2(2\mathcal{N} + 1)$ of the lossy TMST symmetric (green) and asymmetric (purple) states. (c) Probability of successful two-photon subtraction applied to lossy TMST symmetric (blue dashed) and asymmetric (red dashed) states, represented against the fidelity gain compared to the lossy TMST state, which is weighted to be larger for larger fidelities. (d) Efficiency of two-photon subtraction against the transmissivity, with $\tau \in [0.9, 1]$, applied to TMST symmetric (blue dashed) and asymmetric (red dashed) states, at $x = 0$. In panels (e) and (f), we represent the logarithmic negativity $E_{\mathcal{N}} = \log_2(2\mathcal{N} + 1)$ of entangled resources distributed through open air, represented against the traveled distance. (e) We subtract the logarithmic negativity of the lossy TMST symmetric (TMST sym, in green) state from those of the probabilistic (dashed) and heuristic (solid) re-Gaussified two-photon-subtracted symmetric states (2PS sym, in blue). (f) We subtract the logarithmic negativity of the lossy TMST asymmetric (TMST asym, in purple) state from those of the probabilistic (dashed) and heuristic (solid) re-Gaussified two-photon-subtracted asymmetric states (2PS asym, in red). Any point above the green (purple) line represents an improvement in negativity for the re-Gaussified photon-subtracted symmetric (asymmetric) states. Parameters are $n = 10^{-2}$, $N_{\mathrm{th}} = 1250$, $r = 1$, $\mu = 1.44 \times 10^{-6}$ m^{-1}, $\eta_{\mathrm{ant}} = 0$, $\tau = 0.95$.

$$\frac{1}{\sqrt{\det[\mathbb{1}_2+\tilde{\Gamma}/2]}}=\frac{1}{2}\left[1+\tau\frac{-\alpha\beta+(1+\gamma)^2+((1-\alpha)(1-\beta)-\gamma^2)\tau}{(1+\alpha)(1+\beta)-\gamma^2-(\alpha\beta-(1-\gamma)^2)\tau}\right], \tag{52}$$

$$1+g=\frac{1}{2}\left[1+\tau\frac{-\alpha\beta+(1+\gamma)^2+((1-\alpha)(1-\beta)-\gamma^2)\tau}{(1+\alpha)(1+\beta)-\gamma^2-(\alpha\beta-(1-\gamma)^2)\tau}\right]^2 \times\left[1+\frac{(1-\alpha\beta+\gamma^2)^2-(\alpha-\beta)^2+4\gamma^2+4\gamma((1-\alpha)(1-\beta)-\gamma^2)\tau}{(1-\alpha\beta+\gamma^2+((1-\alpha)(1-\beta)-\gamma^2)\tau)^2-(\alpha-\beta)^2+4\gamma^2}\right]. \tag{53}$$

If we define a matrix $G=(1+g)\mathbb{1}_2$ with $G^{-1}=\mathbb{1}_2/(1+g)$, then we can write $1+g=\sqrt{\det G}$, which leads to

$$\frac{1+g}{\sqrt{\det[\mathbb{1}_2+\tilde{\Gamma}/2]}}=\frac{1}{\sqrt{\det[(\mathbb{1}_2+\tilde{\Gamma}/2)G^{-1}]}}. \tag{54}$$

By rearranging the terms resulting from the matrix product, we can obtain

$$\left(\mathbb{1}_2+\frac{1}{2}\tilde{\Gamma}\right)G^{-1}=\mathbb{1}_2+\frac{1}{2}\left(\frac{\tilde{\Gamma}-2g\mathbb{1}_2}{1+g}\right)\equiv\mathbb{1}_2+\frac{1}{2}\tilde{\tilde{\Gamma}}, \tag{55}$$

where we have defined $\tilde{\tilde{\Gamma}}=(\tilde{\Gamma}-2g\mathbb{1}_2)/(1+g)$. Now, we want to incorporate the non-Gaussian corrections into the covariance matrix of the effective Gaussian state by using the formula

$$\tilde{\tilde{\Gamma}}=\sigma_z\tilde{\tilde{\Sigma}}_A\sigma_z+\tilde{\tilde{\Sigma}}_B-\sigma_z\tilde{\tilde{\varepsilon}}_{AB}-\tilde{\tilde{\varepsilon}}_{AB}^{\intercal}\sigma_z. \tag{56}$$

We refer to the resulting state as the "re-Gaussified" state. Then, we define

$$\tilde{\tilde{\Sigma}}_A=\frac{1}{1+g}(\tilde{\Sigma}_A-g\mathbb{1}_2), \tag{57a}$$

$$\tilde{\tilde{\Sigma}}_B=\frac{1}{1+g}(\tilde{\Sigma}_B-g\mathbb{1}_2), \tag{57b}$$

$$\tilde{\tilde{\varepsilon}}_{AB}=\frac{1}{1+g}\tilde{\varepsilon}_{AB}. \tag{57c}$$

These represent the submatrices of a covariance matrix $\tilde{\tilde{\Sigma}}$ if

$$|\sqrt{\det\tilde{\Sigma}}-g(2+\tilde{\alpha}+\tilde{\beta})-1|\geq(1+g)|\tilde{\alpha}-\tilde{\beta}| \tag{58}$$

is satisfied. This condition both ensures the positivity of the covariance matrix and that the uncertainty relation is satisfied. For this, we have assumed that $\tilde{\Sigma}_A=\tilde{\alpha}\mathbb{1}_2$, $\tilde{\Sigma}_B=\tilde{\beta}\mathbb{1}_2$, and $\tilde{\varepsilon}_{AB}=\tilde{\gamma}\sigma_z$. The problem is that this convention only works for the symmetric state, and not for the asymmetric one. For the latter, we write

$$\tilde{\tilde{\Sigma}}_A=\frac{1}{1+g}(\tilde{\Sigma}_A-kg\mathbb{1}_2), \tag{59a}$$

$$\tilde{\tilde{\Sigma}}_B=\frac{1}{1+g}(\tilde{\Sigma}_B-(2-k)g\mathbb{1}_2), \tag{59b}$$

$$\tilde{\tilde{\varepsilon}}_{AB}=\frac{1}{1+g}\tilde{\varepsilon}_{AB}. \tag{59c}$$

Since we have seen that a symmetric re-Gaussified state is viable, we impose the same balanced partition on the re-Gaussification of the asymmetric state. From $\tilde{\tilde{\Sigma}}_A=\tilde{\tilde{\Sigma}}_B$, we obtain $k=1+(\tilde{\alpha}-\tilde{\beta})/2g$, which leads to the submatrices

$$\tilde{\tilde{\Sigma}}_A=\frac{1}{1+g}\left(\frac{\tilde{\Sigma}_A+\tilde{\Sigma}_B}{2}-g\mathbb{1}_2\right), \tag{60a}$$

$$\tilde{\tilde{\Sigma}}_B=\frac{1}{1+g}\left(\frac{\tilde{\Sigma}_A+\tilde{\Sigma}_B}{2}-g\mathbb{1}_2\right), \tag{60b}$$

$$\tilde{\tilde{\varepsilon}}_{AB}=\frac{1}{1+g}\tilde{\varepsilon}_{AB}. \tag{60c}$$

The condition these terms need to satisfy is

$$\left|\sqrt{\det\tilde{\Sigma}}+\tfrac{1}{4}(\tilde{\alpha}-\tilde{\beta})^2-g(\tilde{\alpha}+\tilde{\beta})+g^2-1\right|\geq 0, \tag{61}$$

which is naturally met. In Appendix D, a graphical proof that these conditions are met is provided.

As a result of these redefinitions, we effectively mask the non-Gaussian corrections in the expression of the fidelity as further corrections to the submatrices of the covariance matrix of an entangled resource, which is now Gaussian, while maintaining the same fidelity we obtained with the photon-subtracted states. This treatment has shown that we are using a resource that, in the regions in which photon subtraction is beneficial, shows higher entanglement than the bare resource, as expected. In Figs. 10(e) and 10(f), we subtract the logarithmic negativity $E_{\mathcal{N}}=\log_2(2\mathcal{N}+1)$ of the bare resource (TMST) from those of

the heuristic (solid) and the probabilistic (dashed) two-photon-subtracted states. In Fig. 10(e), we display the symmetric states, and in Fig. 10(f), the asymmetric ones. Note that the gain in negativity is lost around the same points as the gain in fidelity. As discussed above, the fidelities corresponding to the symmetric and asymmetric states are equal at first order in $\mu L \ll 1$, and the same behavior can be observed initially in the negativities of both states [see Fig. 10(b)]. However, while the points at which the fidelities of the symmetric and asymmetric states reach the classical limit differs by centimeters, the points at which entanglement is lost for these states differ by tens of meters. This region where negativity is lost is highlighted with a pale red background. Although the entanglement in the asymmetric state reaches further, the symmetric photon-subtraction protocol we envision works better when applied on the symmetric state. The logarithmic negativity of heuristic photon-subtracted states presents a 46% increase with respect to the value for the bare state at $x = 0$, while probabilistic photon-subtracted states only present an initial gain of 28%.

D. Fidelity with entanglement swapping

We consider the case in which both Alice and Bob produce two-mode squeezed states, and each sends one mode to Charlie, who is equidistantly located from the two parties. Then, he performs entanglement swapping using the two modes he has received, which have been degraded by thermal noise and photon losses. If Alice and Bob use the remaining entangled resource they share for teleporting an unknown coherent state, the fidelity of the protocol will be given by

$$\overline{F}_{\mathrm{ES}} = \frac{1}{1+\alpha-\gamma^2/\beta}, \tag{62}$$

where now we have

$$\alpha = (1+2n)\cosh 2r, \tag{63a}$$

$$\beta = (1+2N_{\mathrm{th}})\eta_{\mathrm{eff}} + (1+2n)(1-\eta_{\mathrm{eff}})\cosh 2r, \tag{63b}$$

$$\gamma = (1+2n)\sqrt{1-\eta_{\mathrm{eff}}}\sinh 2r, \tag{63c}$$

and $\eta_{\mathrm{eff}} = 1 - e^{-\mu L/2}(1-\eta_{\mathrm{ant}})$, since the total distance has been reduced by half due to the presence of a third, equidistant party.

This fidelity is represented as the orange curve in Fig. 9, where it shows a gain in fidelity for large distances, right before the classical limit of $\overline{F} = 0.5$ is reached. The extended distance represents 14% of the maximum distance for the bare TMST state. This will be advantageous when the distance at which the classical limit occurs can be extended, for example in the case of quantum communication between satellites.

VI. INTERSATELLITE QUANTUM COMMUNICATION MODEL

An important application of the protocols and the technology addressed in this manuscript is quantum communication between satellites [72,73,105]. Given the security inherent to quantum-based communication protocols, many of the motivations for the use of submillimeter microwaves, i.e., frequencies in the range 30–300 GHz, which is a trend in classical communication between satellites orbiting low earth orbits (LEOs), fade away, and it seems reasonable to aim at maximizing the distances between linked satellites [64]. We consider a greatly simplified model for free-space microwave communication, assuming unpolarized signals and hence ignoring the effects of scintillation and polarization rotation, among others. This means that, whenever we discuss entanglement, it will be understood that we are talking about particle number entanglement. Polarization entanglement, even if perhaps more natural when considering the physics of antennae, is lost whenever the signal enters a coplanar waveguide, hence making it not a good candidate for quantum communication between one-dimensional superconducting chips. Moreover, we assume that the communication is done within the same altitude, i.e., that the two satellites are in similar orbits, which is typically the case when building satellite constellations. This means that the atmospheric absorption, if any, will remain constant during the time of flight of the signals. Additionally, we ignore Doppler effects caused by relative speeds between the orbits.

There are four main families of satellite orbits: GEO, HEO, MEO, and LEO, corresponding to geosynchronous, high, medium, and low earth orbits, respectively. It is customary to define LEOs as orbits with altitudes in the range 700–2000 km; MEOs would then range between 2000–35 786 km; and HEOs in 35 786–$d_M/2$, where d_M is the distance from the Earth to the Moon. The seemingly arbitrary altitude separating MEOs and HEOs is actually the average altitude for which the period equals one sidereal day (23 h 56 m 4 s), and this is precisely where GEOs sit. This altitude is more than 3 times the point at which the exosphere, the last layer of the atmosphere, is observed to fade. GEOs and HEOs are hence "true" free-space orbits, in the sense that there is hardly any gas, and temperature is dominated by the cosmic microwave background—which peaks at 2.7 K. The MEO region is the least populated one, since it is home to the Van Allen belts, which contain charged particles moving at relativistic speeds due to the magnetic field of the Earth, and that can destroy unshielded objects. LEOs, on the other hand, are "cheap" orbits, where most of the satellites orbiting our planet live. Their low altitudes simplify the problems arising from delays between earth-based stations and the satellites.

In this section we will be concerned only with two satellites orbiting either the same GEO or the same LEO, as a simple case study of expected losses and entanglement degradation. There are essentially two kinds of loss one must take into account: atmospheric loss and free-space path loss (FSPL). Total loss will then be simply given by

$$L = L_{\mathrm{A}} L_{\mathrm{FSPL}}. \tag{64}$$

Atmospheric absorption loss is caused by light-matter interactions. These strongly depend on the altitude of the orbits considered, among other parameters such as polarization, frequency, or weather conditions. Atmospheric loss can range from almost negligible (up in the exosphere and beyond) to very significant in the lower layers of the atmosphere, especially when water droplets and dust are present. Atmospheric loss has to be taken into account when considering the case of up- and downlinks, i.e., when linking a satellite with an earth-based station. However, for relatively high altitudes—that is, any altitude where there are satellites—absorption loss is so low in microwaves that it can be taken to vanish as a first approximation, so we set $L_A = 1$.

FSPL is due to the inevitable spreading of a signal in three dimensions; they are often referred to as geometric losses. FSPL is maximal when there is no beam-constraining mechanism, such as a wave guide, or a set of focalizing lenses, i.e., when the signal spreads isotropically: $L_{\mathrm{FSPL}} = (\lambda/4\pi d)^{-2}$.

Suppose that two comoving satellites are separated by a linear distance d, and that the emitter sends a quasi-monochromatic signal with power P_e centered at frequency $\nu = \omega/2\pi = c/\lambda$. The receiver gets a power P_r such that their ratio defines a transmission coefficient that is the product of the loss and gains (or directivities) of the antennae. The resulting equation for long, "far-field" distances is sometimes referred to as Friis' equation [106–108], which is the compromise between gain (or directivity) and loss:

$$\frac{P_e}{P_r} = \frac{D_e D_d}{L_{\mathrm{A}} L_{\mathrm{FSPL}}} = D_e D_r \left(\frac{\lambda}{4\pi d}\right)^2 \equiv \breve{\tau}_{\mathrm{path}}. \tag{65}$$

Here D_e and D_r are the directivities of the emitter and receiver antennas, and we set $L_A = 1$ as discussed before. The directivity of an antenna is the maximized gain in power in some preferred direction with respect to a hypothetical isotropic antenna, at a fixed distance from the source, and assuming that the total radiation power is the same for both antennas: $D = \max_{\theta,\phi} D(\theta,\phi)$. It is a quantity that strongly depends on the geometry design, but that can be enhanced in a discrete fashion by means of antenna arrays. Indeed, given N identical antennas with directivity gain $D(\theta,\phi)$, a phased array consists of an array of such antennas, each preceded by a controlled phase shifter. This diffraction problem essentially gives $D_{\mathrm{array}}(\theta,\phi) = A_N^2(\boldsymbol{\varepsilon}) D(\theta,\phi)$, where A_N is the so-called N-array factor that symbolically depends on the phases via some vector $\boldsymbol{\varepsilon}$ [109]. In three dimensions, phase arrays are two-dimensional grids of antennas, so that the main lobe of the resulting signal becomes as sharp as possible. We assume that we have an array of small coplanar antennas as discussed in Sec. III B, adding up to a radiation pattern mimicking that of a parabolic antenna. We also assume that both emitter and receiver have the same design, $D_e = D_r \equiv D$ with

$$D = \left(\frac{\pi a}{\lambda}\right)^2 e_a, \tag{66}$$

where $0 \leq e_a \leq 1$ is the aperture efficiency, defined as the ratio between the effective aperture A_e and the area of the antenna's actual aperture A_{phys}, and a is the diameter of the parabola, such that $A_{\mathrm{phys}} = \pi a^2/4$. With this, the parabolic path transmissivity becomes

$$\breve{\tau}_{\mathrm{path}} = \left(\frac{\pi a^2 e_a}{4 d \lambda}\right)^2. \tag{67}$$

The effect of path losses can alternatively be described by a diffraction mechanism, affecting the spot size of the signal beam,

$$\varpi = \frac{\varpi_0}{\sqrt{2}} \sqrt{\left(1 - \frac{d}{R_0}\right)^2 + \left(\frac{d}{d_R}\right)^2}, \tag{68}$$

given an initial spot size ϖ_0, curvature of the beam R_0, and Rayleigh range $d_R = \pi \varpi_0^2 \lambda^{-1}/2$. Given the aperture radius a_R of the receiver antenna, the diffraction-induced transmissivity can be computed as [72,73]

$$\breve{\tau}_{\mathrm{diff}} = 1 - e^{-2a_R^2/\varpi^2}. \tag{69}$$

Note that, in the far-field approximation, we can recover the result for $\breve{\tau}_{\mathrm{path}}$,

$$\breve{\tau}_{\mathrm{diff}} \approx \left(\frac{\pi \varpi_0 a_R}{\lambda d}\right)^2, \tag{70}$$

by setting $a_R = \varpi_0 = a/2$, $R_0 = d$, and assuming that $e_a = 1$. Setting $\lambda = 6$ cm and $a_R = 2\varpi_0$, we plot the transmissivity associated with diffraction versus the distance d for different values of the aperture ϖ_0 in Fig. 11(a), observing that losses are reduced as a result of an increase in the aperture.

We address entanglement preservation in TMST states distributed through open air by considering that the dominant source of error will be diffraction, as opposed to attenuation, which we describe by means of a beam splitter with a thermal input. We introduce $N_{\mathrm{th}} \sim 11$ as the

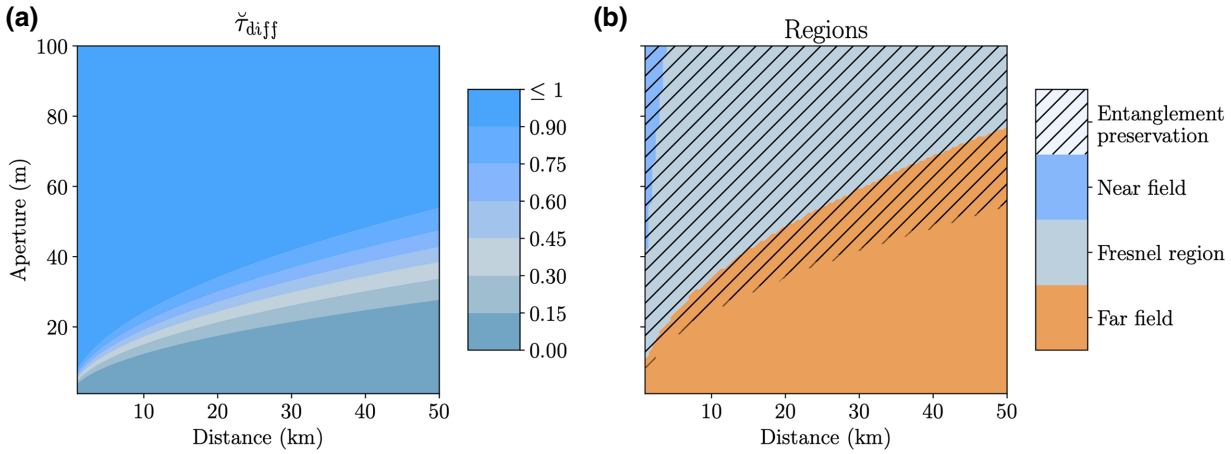

FIG. 11. (a) Contour plot of the transmissivity associated with diffraction, $\breve{\tau}_{\mathrm{diff}}$, against the aperture radius of the antenna and the traveled distance. We can observe that losses are greatly reduced with the aperture of the antenna. (b) Contour plot of the regions of free space as delimited by the relation between the aperture radius of the antenna and the distance at which the signal is observed: near field (blue) $\varpi_0 > (\lambda d/0.62)^{2/3}$, Fresnel (gray) $\sqrt{\lambda d/2} < \varpi_0 < (\lambda d/0.62)^{2/3}$, and far field (orange) $\varpi_0 < \sqrt{\lambda d/2}$. With dashed lines, we represent the region where entanglement can be preserved. Parameters are $\lambda = 6$ cm, $a_R = 2\varpi_0$.

number of thermal photons in the environment at 2.7 K. Considering this loss mechanism, entanglement preservation is achieved for reflectivities that satisfy $\eta < (1 + N_{\mathrm{th}})^{-1} \sim 0.083$ for lossy TMST asymmetric states and $\eta < [1 + N_{\mathrm{th}}(1 + \coth r)]^{-1} \sim 0.038$ for symmetric states, assuming that $n \approx 0$ and $\breve{\tau} = 1 - \eta$. Given this diffraction channel, entanglement is preserved in the regime $a_R\varpi_0/d > (\lambda/\pi)\sqrt{-\log \eta_{\mathrm{lim}}} \sim 0.035$ for $\lambda = 6$ cm and $\eta_{\mathrm{lim}} = 0.038$. This implies that, for two satellites that are separated by $d = 1$ km, the product of the apertures of emitter and receiver antennae must be $a_R\varpi_0 > 35\ \mathrm{m}^2$ in order to have entanglement preservation. In Fig. 11(b), we represent the regions of free space as delimited by the relation between the distance at which the signal is detected and the aperture of the emitting antenna, taking $a_R = 2\varpi_0$, and depicting the region in which entanglement is preserved with a dashed line. This shows that the radius of the antennae of emitter and receiver satellites will be large, as is usually the case for microwave communications. In order to correct the effects of diffraction with microwaves, it would also be useful to study focalizing techniques and the incorporation of beam collimators.

VII. CONCLUSIONS

In this manuscript, we study the feasibility of microwave entanglement distribution in open air with two-mode squeezed states. We study these as a resource for the Braunstein-Kimble quantum-teleportation protocol adapted to microwave technology, reviewing the steps involved in this process and the possible experimental realization. First, we review the generation of two-mode squeezed states using JPAs that was experimentally demonstrated in Ref. [69]. Then, we look at an antenna model [86] for optimal transmission of these states into open air, while also discussing the maximum possible reach of entanglement and its degradation due to interactions with the environment. The reach is found to extend up to 550 m for asymmetric states with ideal weather conditions. We adapt entanglement distillation and entanglement swapping to microwave technology to counteract degradation at different stages. In particular, we study photon subtraction, an entanglement distillation protocol that works for short distances and low squeezing, allowing up to a 46% increase in the logarithmic negativity. Entanglement distillation, on the other hand, contributes to extending the reach of entanglement by up to 14%. Since these operations require homodyne detection, as well as photocounting, we discuss recent advances in microwave technologies that permit these operations. We then test the efficiency of open-air entanglement distribution, including the different enhancement techniques, with the Braunstein-Kimble protocol adapted to microwaves: we compute the average fidelities of open-air microwave quantum teleportation of coherent states using the open-air-distributed states as the entangled resource. We conclude with a study of the applicability and efficiency of these techniques for quantum communication between satellites, a field where, with the proper directivity, the reach of entanglement can be greatly increased, given the low absorption rates.

Efficient information retrieval from an open-air distribution of microwave quantum states is a key component of open-air quantum communications, which requires the design of a receiver antenna. The device achieving this target may resemble that in Sec. III B, but it calls for a different type of termination into open air in order to, for instance, reduce diffraction losses. Since the lack of an amplification protocol considerably limits the

entanglement transmission distance through open air, it seems necessary to develop a theory of quantum repeaters for microwave signals, following the ideas shown in Ref. [70]. To this end, entanglement distillation and entanglement swapping techniques discussed in this manuscript are useful.

Since superconducting circuits naturally work in the microwave regime, it is desirable to explore realizations of photon subtraction that use devices specific to this technology. In particular, a possible deterministic photon-subtraction scheme can be studied, making use of circuit QED for nondemolition detection of itinerant microwave photons [101]. In this paper, the detection of a previously unknown microwave photon is triggered by a transmon qubit jumping to its excited state, indicating a successful photon-subtraction event.

ACKNOWLEDGMENTS

The authors thank R. Assouly, R. Dassonneville, and B. Huard for useful discussions. All authors acknowledge support from QMiCS (Grant No. 820505) of the EU Flagship on Quantum Technologies. T.G.-R. and M.S. acknowledge financial support from the Basque Government QUANTEK project under the ELKARTEK program (KK-2021/00070), the Spanish Ramón y Cajal Grant No. RYC-2020-030503-I, project Grant No. PID2021-125823NA-I00 funded by MCIN/AEI/10.13039/501100011033 and by "ERDF A way of making Europe" and "ERDF Invest in your Future", OpenSuperQ (820363) of the EU Flagship on Quantum Technologies, the EU FET-Open projects Quromorphic (828826) and EPIQUS (899368), and IQM Quantum Computers under the project "Generating quantum algorithms and quantum processor optimization". M.C. and Y.O. thank the support from FCT – Fundação para a Ciência e a Tecnologia (Portugal), namely through project UIDB/04540/2020, as well as from project TheBlinQC supported by the EU H2020 QuantERA ERA-NET Cofund in Quantum Technologies and by FCT (QuantERA/0001/2017). M.C. acknowledges support from the DP-PMI and FCT through scholarship PD/BD/135186/2017. M.R., F.F., F.D., and K.F. acknowledge support from the German Research Foundation via Germany's Excellence Strategy (EXC-2111-390814868), Elite Network of Bavaria through program ExQM, and the German Federal Ministry of Education and Research via project QUARATE (Grant No. 13N15380) and project QuaMToMe (Grant No. 16KISQ036). This research is part of the Munich Quantum Valley, which is supported by the Bavarian state government with funds from the Hightech Agenda Bayern Plus. The research of V.S. is supported by the Basque Government through the BERC 2022–2025 program and by the Ministry of Science, Innovation, and Universities: BCAM Severo Ochoa accreditation SEV-2017-0718. M.M. acknowledges funding from the European Research Council under Consolidator Grant No. 681311 (QUESS), from the Jane and Aatos Erkko Foundation and the Technology Industries of Finland Centennial Foundation through their Future Makers program, and from the Academy of Finland through its Centers of Excellence Program (Projects No. 312300 and No. 336810).

APPENDIX A: AMPLIFICATION

In this manuscript, we have not discussed an amplification protocol for entangled signals because it cannot increase quantum correlations. Amplification of signals is an essential feature in classical microwave communication in open air, as increasing the number of photons that Alice sends will improve the chances Bob has of detecting that signal. In the quantum regime, cryogenic high electronic mobility transistor (HEMT) amplifiers are suited for experiments with microwaves. These are able to greatly enhance signals in a large frequency spectrum, while introducing a significant amount of thermal photons. This noise is reflected in the input-output relation

$$a_{\text{out}} = \sqrt{g_H}\, a_{\text{in}} + \sqrt{g_H - 1}\, h_H \tag{A1}$$

with a_{in}, a_{out}, and h_H the annihilation operators of the input field, output field, and noise added by the amplifier, respectively. From this formula, we can see that amplification is a procedure that acts individually on the modes of a quantum state, which means that we can increment the number of photons of that mode, but they will not be entangled with the other ones. That is why we say that amplification cannot increase quantum correlations. If anything, the introduction of thermal noise can lead to entanglement degradation.

HEMTs normally work at 4 K temperatures, which implies that the number of thermal photons they introduce is around $n_H \sim 10$–20 for 5 GHz frequencies. It is the number of thermal photons that determines the thermally radiated power [110], $P = \hbar\omega NB$, meaning that the excess output noise produces a flux of N photons per second in a bandwidth of B Hz. The gain is given by the ratio between output and input powers, and for a constant bandwidth, it is just $g_H = n_H/n$, the ratio between the number of thermal photons introduced by the HEMT and the number of photons in the input state. Considering the antenna described above, a HEMT of these characteristics produces a gain of $g_H = 2 \times 10^3$ when acting on a TMST state with $n \sim 10^{-2}$, which completely destroys entanglement. In order for entanglement to survive such an amplification process, the HEMT must be placed at temperatures below 100 mK. In any case, they do not present an advantage.

APPENDIX B: HEURISTIC PHOTON SUBTRACTION

In this section, we describe the heuristic photon-subtraction operation, in which annihilation operators are applied to a quantum state in order to reduce the number of photons in each mode. Consider that we initially have a TMSV state,

$$|\psi\rangle_{AB} = \sqrt{1-\lambda^2}\sum_{n=0}^{\infty}\lambda^n|n,n\rangle_{AB} \tag{B1}$$

with $\lambda = \tanh r$ and squeezing parameter r. Assume that we apply the operator $a_A^k a_B^l$, which implies subtracting k photons in mode A and l photons in mode B. The resulting state is

$$|\psi^{(k+l)}\rangle_{AB} = \sqrt{1-\lambda^2} \times \sum_{n=\max\{k,l\}}^{\infty}\frac{\lambda^n n!}{\sqrt{(n-k)!\,(n-l)!}}|n-k,n-l\rangle_{AB}. \tag{B2}$$

Considering symmetric photon subtraction ($k = l$), we can write this state as

$$|\psi^{(2k)}\rangle_{AB} = \sqrt{1-\lambda^2}\sum_{n=0}^{\infty}\frac{\lambda^{n+k}(n+k)!}{n!}|n,n\rangle_{AB}, \tag{B3}$$

where we have shifted $n \to n+k$. This state needs to be normalized, and the normalization is given by

$$\begin{aligned} N_{2k} &= (1-\lambda^2)\lambda^{2k}(k!)^2\sum_{n=0}^{\infty}\lambda^{2n}\binom{n+k}{k}^2 \\ &= (1-\lambda^2)\lambda^{2k}(k!)^2\,{}_2F_1(k+1,k+1;1;\lambda^2). \end{aligned} \tag{B4}$$

The negativity of this state can be computed as

$$\mathcal{N}(\rho^{(2k)}) = \frac{A_k - 1}{2} \tag{B5}$$

with $\rho^{(2k)} = |\psi^{(2k)}\rangle\langle\psi^{(2k)}|$ and

$$A_k \equiv \left(\sqrt{\frac{1-\lambda^2}{N_{2k}}}\sum_{n=0}^{\infty}\lambda^{n+k}\frac{(n+k)!}{n!}\right)^2. \tag{B6}$$

This leads to

$$\mathcal{N}(\rho^{(2k)}) = \frac{1}{2}\left(\frac{(1-\lambda)^{-2(k+1)}}{{}_2F_1(k+1,k+1;1;\lambda^2)} - 1\right), \tag{B7}$$

from which we can recover the negativity of the TMSV state by setting $k = 0$:

$$\mathcal{N}(\rho^{(0)}) = \frac{\lambda}{1-\lambda} = \frac{e^{2r}-1}{2}. \tag{B8}$$

Now, we go beyond the TMSV state case, and explore the heuristic photon-subtraction protocol applied on a general Gaussian state. The application of the single-photon annihilation operators on both modes of a bipartite quantum state ρ is equivalent to applying

$$\Theta_1\Theta_2\chi(\alpha,\beta) \tag{B9}$$

to its the characteristic function [80], with

$$\Theta_i = \partial_{x_i^2} + \partial_{p_i^2} + \frac{x_i^2}{4} + \frac{p_i^2}{4} + x_i\partial_{x_i} + p_i\partial_{p_i} + 1 \tag{B10}$$

for $i = \{1,2\}$. Given that $\rho = (1/\pi^2)\int \mathrm{d}^2\alpha \int \mathrm{d}^2\beta\,\chi(\alpha,\beta)$ $D_1(-\alpha)D_2(-\beta)$, and assuming that ρ is a Gaussian state with covariance matrix

$$\Sigma = \begin{pmatrix} \Sigma_A & \varepsilon_{AB} \\ \varepsilon_{AB}^{\intercal} & \Sigma_B \end{pmatrix}, \tag{B11}$$

then we can write

$$\begin{aligned} \Theta_1\Theta_2\chi(\alpha,\beta) = N[&(m_B + \vec{\beta}M_B\vec{\beta}^{\intercal} + \vec{\alpha}M_{BC}\vec{\beta}^{\intercal} + \vec{\alpha}M_C\vec{\alpha}^{\intercal})(m_A + \vec{\alpha}M_A\vec{\alpha}^{\intercal} + \vec{\alpha}M_{AC}\vec{\beta}^{\intercal} + \vec{\beta}M_C\vec{\beta}^{\intercal}) + m_C - \vec{\alpha}M_{AC}\Omega\varepsilon_{AB}\Omega^{\intercal}\vec{\alpha}^{\intercal} \\ &+ 2\vec{\beta}M_C(\mathbb{1}_2 - \Omega\Sigma_B\Omega^{\intercal})\vec{\beta}^{\intercal} + \vec{\alpha}[M_{AC}(\mathbb{1}_2 - \Omega\Sigma_B\Omega^{\intercal}) - \Omega\varepsilon_{AB}\Omega^{\intercal}M_C]\vec{\beta}^{\intercal}]\chi(\alpha,\beta), \end{aligned} \tag{B12}$$

where we have defined

$$
\begin{aligned}
m_A &= 1 - \tfrac{1}{2}\mathrm{tr}\Sigma_A,\\
m_B &= 1 - \tfrac{1}{2}\mathrm{tr}\Sigma_B,\\
m_C &= \tfrac{1}{2}\mathrm{tr}\left(\varepsilon_{AB}^{\intercal}\varepsilon_{AB}\right)\\
M_A &= \tfrac{1}{4}(\mathbb{1}_2 - 2\Omega\Sigma_A\Omega^{\intercal} + \Omega\Sigma_A^2\Omega^{\intercal}),\\
M_B &= \tfrac{1}{4}(\mathbb{1}_2 - 2\Omega\Sigma_B\Omega^{\intercal} + \Omega\Sigma_B^2\Omega^{\intercal}),\\
M_C &= \tfrac{1}{4}\Omega\varepsilon_{AB}^{\intercal}\varepsilon_{AB}\Omega^{\intercal},\\
M_{AC} &= \tfrac{1}{2}(\Omega\Sigma_A\varepsilon_{AB}\Omega^{\intercal} - \Omega\varepsilon_{AB}\Omega^{\intercal}),\\
M_{BC} &= \tfrac{1}{2}(\Omega\varepsilon_{AB}\Sigma_B\Omega^{\intercal} - \Omega\varepsilon_{AB}\Omega^{\intercal}).
\end{aligned}
$$

Here, $N^{-1} = m_A m_B + m_C$ is a normalization constant, which enforces $\Theta_1\Theta_2\chi(\alpha,\beta)|_{\alpha=0,\beta=0} = 1$. Keep in mind that we have assumed that the submatrices Σ_A, Σ_B, and ε_{AB} of the covariance matrix are symmetric.

If we use these states as the entangled resource on a CV quantum teleportation protocol of an unknown coherent state, the average fidelity can be written as

$$
\overline{F} = \frac{1+h}{\sqrt{\det[\mathbb{1}_2 + \Gamma/2]}} \tag{B13}
$$

with $\Gamma \equiv \sigma_Z\Sigma_A\sigma_Z + \Sigma_B - \sigma_Z\varepsilon_{AB} - \varepsilon_{AB}^{\intercal}\sigma_Z$. Here, we have defined h as

$$
\begin{aligned}
h = \frac{1}{E_0}\Bigg\{ &\mathrm{tr}\left[\Omega\left(\mathbb{1}_2 + \frac{1}{2}\Gamma\right)^{-1}\Omega^{\intercal}E_1\right]\\
&- \frac{2}{\det(\mathbb{1}_2 + \Gamma/2)}\mathrm{tr}(\Omega E_2^A\Omega^{\intercal}E_2^B)\\
&+ 3\mathrm{tr}\left[\Omega\left(\mathbb{1}_2 + \frac{1}{2}\Gamma\right)^{-1}\Omega^{\intercal}E_2^A\right]\\
&\times \mathrm{tr}\left[\Omega\left(\mathbb{1}_2 + \frac{1}{2}\Gamma\right)^{-1}\Omega^{\intercal}E_2^B\right]\Bigg\},
\end{aligned} \tag{B14}
$$

together with

$$
E_0 = m_A m_B + m_C, \tag{B15a}
$$

$$
\begin{aligned}
E_1 = {}& m_A(M_B + \sigma_z M_C\sigma_z + \sigma_z M_{BC})\\
&+ m_B(\sigma_z M_A\sigma_z + M_C + \sigma_z M_{AC})\\
&+ (2M_C + \sigma_z M_{AC})\Omega(\mathbb{1}_2 + \sigma_z\varepsilon_{AB} - \Sigma_B)\Omega^{\intercal},
\end{aligned} \tag{B15b}
$$

$$
E_2^A = M_C + \sigma_z M_{AC} + \sigma_z M_A\sigma_z, \tag{B15c}
$$

$$
E_2^B = M_B + \sigma_z M_{BC} + \sigma_z M_C\sigma_z. \tag{B15d}
$$

We can identify h as the non-Gaussian corrections to the fidelity, and mask them as corrections to the covariance matrix of a Gaussian state with the same fidelity. This is done by defining

$$
\tilde{\Gamma} = \frac{\Gamma - 2h\mathbb{1}_2}{1+h} \equiv \sigma_Z\tilde{\Sigma}_A\sigma_Z + \tilde{\Sigma}_B - \sigma_Z\tilde{\varepsilon}_{AB} - \tilde{\varepsilon}_{AB}^{\intercal}\sigma_Z. \tag{B16}
$$

For the symmetric resource, we define

$$
\tilde{\Sigma}_A = \frac{1}{1+h}(\Sigma_A - h\mathbb{1}_2), \tag{B17a}
$$

$$
\tilde{\Sigma}_B = \frac{1}{1+h}(\Sigma_B - h\mathbb{1}_2), \tag{B17b}
$$

$$
\tilde{\varepsilon}_{AB} = \frac{1}{1+h}\varepsilon_{AB}, \tag{B17c}
$$

whereas for the asymmetric one, we require that $\tilde{\Sigma}_A = \tilde{\Sigma}_B$, such that

$$
\tilde{\Sigma}_A = \frac{1}{1+h}\left(\frac{\Sigma_A + \Sigma_B}{2} - h\mathbb{1}_2\right), \tag{B18a}
$$

$$
\tilde{\Sigma}_B = \frac{1}{1+h}\left(\frac{\Sigma_A + \Sigma_B}{2} - h\mathbb{1}_2\right), \tag{B18b}
$$

$$
\tilde{\varepsilon}_{AB} = \frac{1}{1+h}\varepsilon_{AB}. \tag{B18c}
$$

These "re-Gaussified" covariance matrices need to satisfy positivity and the uncertainty principle, meaning that $|\sqrt{\det\tilde{\Sigma}} - 1| \geq |\tilde{\alpha} - \tilde{\beta}|$, assuming that we can write $\tilde{\Sigma}_A = \tilde{\alpha}\mathbb{1}_2$, $\tilde{\Sigma}_B = \tilde{\beta}\mathbb{1}_2$, and $\tilde{\varepsilon}_{AB} = \tilde{\gamma}\sigma_z$. Furthermore, if $\Sigma_A = \alpha\mathbb{1}_2$, $\Sigma_B = \beta\mathbb{1}_2$, and $\varepsilon_{AB} = \gamma\sigma_z$, this condition can be expressed as

$$
|\sqrt{\det\Sigma} - h(2 + \alpha + \beta) - 1| \geq (1+h)|\alpha - \beta| \tag{B19}
$$

for the symmetric state, and as

$$
\left|\sqrt{\det\Sigma} + \tfrac{1}{4}(\alpha - \beta)^2 - h(\alpha + \beta) + h^2 - 1\right| \geq 0 \tag{B20}
$$

for the asymmetric one. A graphical proof that these conditions are met can be found in Appendix D.

APPENDIX C: PROBABILISTIC PHOTON SUBTRACTION

In this section, we present the definitions we have used to shorten the notation of the modified submatrices of the covariance matrix of a Gaussian state that has undergone a symmetric two-photon-subtraction protocol (with beam splitters and photodetectors). Assuming that Σ_A, Σ_B, and ε_{AB} are symmetric, the general expressions for the submatrices of the covariance matrix of the resulting

state are

$$\tilde{\Sigma}_A = \tau\Sigma_A + (1-\tau)\mathbb{1}_2 - 2(J_1 X_A^{-1} J_1^\intercal + K_1 Y^{-1} K_1^\intercal), \tag{C1a}$$

$$\tilde{\Sigma}_B = \tau\Sigma_B + (1-\tau)\mathbb{1}_2 - 2(J_2 X_A^{-1} J_2^\intercal + K_2 Y^{-1} K_2^\intercal), \tag{C1b}$$

$$\tilde{\varepsilon}_{AB} = \tau\varepsilon_{AB} - 2(J_1 X_A^{-1} J_2^\intercal + K_1 Y^{-1} K_2^\intercal), \tag{C1c}$$

whose success probability is given by

$$P = \frac{m_1 m_2 + m_3}{\sqrt{\det X_A \det Y}}. \tag{C2}$$

Here, we have used

$$\begin{aligned}
X_A &= \tfrac{1}{2}\Omega[(1-\tau)\Sigma_A + (1+\tau)\mathbb{1}_2]\Omega^\intercal,\\
X_B &= \tfrac{1}{2}\Omega[(1-\tau)\Sigma_B + (1+\tau)\mathbb{1}_2]\Omega^\intercal,\\
H &= -\tfrac{1}{2}(1-\tau)\Omega\varepsilon_{AB}\Omega^\intercal,\\
Y &= X_B - H X_A^{-1} H,\\
W_{X,M} &= X^{-1}\mathrm{tr}(X^{-1}M) - \frac{\Omega M \Omega^\intercal}{\det X},\\
m_1 &= 1 - \tfrac{1}{2}\mathrm{tr}Y^{-1},\\
m_2 &= 1 - \tfrac{1}{2}\mathrm{tr}X_A^{-1} - \tfrac{1}{2}\mathrm{tr}(Y^{-1} H W_{X_A,\mathbb{1}_2} H),\\
m_3 &= \tfrac{1}{2}\mathrm{tr}(W_{Y,\mathbb{1}_2} H W_{X_A,\mathbb{1}_2} H),\\
K_1 &= \tfrac{1}{2}\sqrt{\tau(1-\tau)}[\varepsilon_{AB}\Omega^\intercal + (\Sigma_A - \mathbb{1}_2)\Omega^\intercal X_A^{-1} H],\\
K_2 &= \tfrac{1}{2}\sqrt{\tau(1-\tau)}[(\Sigma_B - \mathbb{1}_2)\Omega^\intercal + \varepsilon_{AB}\Omega^\intercal X_A^{-1} H],\\
J_1 &= \tfrac{1}{2}\sqrt{\tau(1-\tau)}(\Sigma_A - \mathbb{1}_2)\Omega^\intercal,\\
J_2 &= \tfrac{1}{2}\sqrt{\tau(1-\tau)}\varepsilon_{AB}\Omega^\intercal.
\end{aligned}$$

The characteristic function of the resulting non-Gaussian state is

$$\begin{aligned}
\chi^{(1,1)}(\alpha,\beta) = \frac{e^{-[\vec{\alpha}\Omega\tilde{\Sigma}_A\Omega^\intercal\vec{\alpha}^\intercal + \vec{\beta}\Omega\tilde{\Sigma}_B\Omega^\intercal\vec{\beta}^\intercal + 2\vec{\alpha}\Omega\tilde{\varepsilon}_{AB}\Omega^\intercal\vec{\beta}^\intercal]/4}}{m_1 m_2 + m_3}&[(m_1 + \vec{\alpha}P_1\vec{\alpha}^\intercal + \vec{\beta}P_2\vec{\beta}^\intercal + \vec{\alpha}P_{12}\vec{\beta}^\intercal)\\
&\times (m_2 + \vec{\alpha}Q_1\vec{\alpha}^\intercal + \vec{\beta}Q_2\vec{\beta}^\intercal + \vec{\alpha}Q_{12}\vec{\beta}^\intercal) + m_3 + \vec{\alpha}R_1\vec{\alpha}^\intercal + \vec{\beta}R_2\vec{\beta}^\intercal + \vec{\alpha}R_{12}\vec{\beta}^\intercal].
\end{aligned} \tag{C3}$$

Furthermore, when computing the average fidelity [Eq. (51)], we obtain the non-Gaussian corrections defined by

$$\begin{aligned}
g = \frac{1}{m_1 m_2 + m_3}&\left[m_1 \mathrm{tr}\left[\Omega\left(\mathbb{1}_2 + \frac{1}{2}\tilde{\Gamma}\right)^{-1}\Omega^\intercal(\sigma_z Q_1 \sigma_z + Q_2 + \sigma_z Q_{12})\right] + m_2 \mathrm{tr}\left[\Omega\left(\mathbb{1}_2 + \frac{1}{2}\tilde{\Gamma}\right)^{-1}\Omega^\intercal(\sigma_z P_1 \sigma_z + P_2 + \sigma_z P_{12})\right]\right.\\
&+ \mathrm{tr}\left[\Omega\left(\mathbb{1}_2 + \frac{1}{2}\tilde{\Gamma}\right)^{-1}\Omega^\intercal(\sigma_z P_1 \sigma_z + P_2 + \sigma_z P_{12})\right]\mathrm{tr}\left[\Omega\left(\mathbb{1}_2 + \frac{1}{2}\tilde{\Gamma}\right)^{-1}\Omega^\intercal(\sigma_z Q_1 \sigma_z + Q_2 + \sigma_z Q_{12})\right]\\
&\left.+ \mathrm{tr}\left[\Omega\left(\mathbb{1}_2 + \frac{1}{2}\tilde{\Gamma}\right)^{-1}\Omega^\intercal(\sigma_z R_1 \sigma_z + R_2 + \sigma_z R_{12})\right] + 2\mathrm{tr}\left[W_{\Omega(\mathbb{1}_2 + \tilde{\Gamma}/2)\Omega^\intercal, \sigma_z P_1 \sigma_z + P_2 + \sigma_z P_{12}}(\sigma_z Q_1 \sigma_z + Q_2 + \sigma_z Q_{12})\right]\right],
\end{aligned} \tag{C4}$$

which can be computed using

$$\begin{aligned}
P_1 &= -\tfrac{1}{2}\Omega K_1 W_{Y,\mathbb{1}_2} K_1^\intercal \Omega^\intercal,\\
P_2 &= -\tfrac{1}{2}\Omega K_2 W_{Y,\mathbb{1}_2} K_2^\intercal \Omega^\intercal,\\
P_{12} &= -\Omega K_1 W_{Y,\mathbb{1}_2} K_2^\intercal \Omega^\intercal,\\
Q_1 &= -\tfrac{1}{2}\Omega(J_1 W_{X_A,\mathbb{1}_2} J_1^\intercal + 2J_1 W_{X_A,\mathbb{1}_2} H Y^{-1} K_1^\intercal + K_1 W_{Y,H W_{X_A,\mathbb{1}_2} H} K_1^\intercal)\Omega^\intercal,\\
Q_2 &= -\tfrac{1}{2}\Omega(J_2 W_{X_A,\mathbb{1}_2} J_2^\intercal + 2J_2 W_{X_A,\mathbb{1}_2} H Y^{-1} K_2^\intercal + K_2 W_{Y,H W_{X_A,\mathbb{1}_2} H} K_2^\intercal)\Omega^\intercal,\\
Q_{12} &= -\Omega(J_1 W_{X_A,\mathbb{1}_2} J_2^\intercal + J_1 W_{X_A,\mathbb{1}_2} H Y^{-1} K_2^\intercal + K_1 Y^{-1} H W_{X_A,\mathbb{1}_2} J_2^\intercal + K_1 W_{Y,H W_{X_A,\mathbb{1}_2} H} K_2^\intercal)\Omega^\intercal,\\
R_1 &= \frac{1}{2}\Omega\left[J_1 W_{X_A,\mathbb{1}_2} H W_{Y,\mathbb{1}_2} K_1^\intercal + K_1\left(W_{Y,\mathbb{1}_2}\mathrm{tr}(Y^{-1} H W_{X_A,\mathbb{1}_2} H) + Y^{-1}\mathrm{tr}(W_{Y,\mathbb{1}_2} H W_{X_A,\mathbb{1}_2} H) - \frac{\Omega H W_{X_A,\mathbb{1}_2} H \Omega^\intercal}{\det Y}\mathrm{tr}Y^{-1}\right)K_1^\intercal\right]\Omega^\intercal,
\end{aligned}$$

$$R_2 = \frac{1}{2}\Omega\left[J_2 W_{X_A,\mathbb{1}_2} H W_{Y,\mathbb{1}_2} K_2^\intercal + K_2\left(W_{Y,\mathbb{1}_2}\mathrm{tr}(Y^{-1}HW_{X_A,\mathbb{1}_2}H) + Y^{-1}\mathrm{tr}(W_{Y,\mathbb{1}_2}HW_{X_A,\mathbb{1}_2}H) - \frac{\Omega H W_{X_A,\mathbb{1}_2} H\Omega^\intercal}{\det Y}\mathrm{tr}Y^{-1}\right)K_2^\intercal\right]\Omega^\intercal,$$

$$R_{12} = \frac{1}{2}\Omega\left[J_1 W_{X_A,\mathbb{1}_2} H W_{Y,\mathbb{1}_2} K_2^\intercal + K_1 W_{Y,\mathbb{1}_2} H W_{X_A,\mathbb{1}_2} J_2^\intercal + 2K_1\left(W_{Y,\mathbb{1}_2}\mathrm{tr}(Y^{-1}HW_{X_A,\mathbb{1}_2}H) + Y^{-1}\mathrm{tr}(W_{Y,\mathbb{1}_2}HW_{X_A,\mathbb{1}_2}H)\right.\right.$$
$$\left.\left. - \frac{\Omega H W_{X_A,\mathbb{1}_2} H\Omega^\intercal}{\det Y}\mathrm{tr}Y^{-1}\right)K_2^\intercal\right]\Omega^\intercal.$$

APPENDIX D: POSITIVITY AND THE UNCERTAINTY PRINCIPLE FOR COVARIANCE MATRICES

In this section, we discuss the conditions that a covariance matrix must satisfy in order for it to describe a quantum state. Then, we apply this criterion to the covariance matrices obtained after photon subtraction and entanglement swapping. The first condition is the positivity of the covariance matrix

$$\Sigma = \begin{pmatrix} \Sigma_A & \varepsilon_{AB} \\ \varepsilon_{AB}^\intercal & \Sigma_B \end{pmatrix} > 0, \tag{D1}$$

and the second one is preservation of the uncertainty principle,

$$\begin{pmatrix} \Sigma_A & \varepsilon_{AB} \\ \varepsilon_{AB}^\intercal & \Sigma_B \end{pmatrix} + i\begin{pmatrix} \Omega & 0 \\ 0 & \Omega \end{pmatrix} \geq 0. \tag{D2}$$

If we consider $\Sigma_A = \alpha\mathbb{1}_2$, $\Sigma_B = \beta\mathbb{1}_2$, and $\varepsilon_{AB} = \gamma\sigma_z$, the positivity condition reduces to

$$\alpha > 0, \quad \det\Sigma > 0, \tag{D3}$$

whereas the uncertainty principle can be written as

$$\alpha \geq 1, \quad \det\Sigma \geq \alpha^2 + \beta^2 - 2\gamma^2 - 1. \tag{D4}$$

Note that the latter imposes a more restrictive condition. Given that any covariance matrix requires $\alpha \geq 1$ and $\beta \geq 1$, we can summarize all conditions as

$$\vartheta \equiv |\sqrt{\det\Sigma} - 1| - |\alpha - \beta| \geq 0. \tag{D5}$$

In Fig. 12, we investigate whether this condition is satisfied for different modified covariance matrices by representing ϑ against the traveled distance: submatrices in Eqs. (39) due to entanglement swapping (orange); in Eqs. (B17) and (B18) due to re-Gaussified heuristic photon subtraction (symmetric shown with a blue solid line, asymmetric shown with a red solid line); in Eqs. (57) and (60) due to re-Gaussified probabilistic photon subtraction (symmetric shown with a blue dashed line, asymmetric shown with a red dashed line). Note that all five cases satisfy both positivity and uncertainty principle conditions, confirming that they are indeed covariance matrices. In the inset, we present an enlarged view of the short distance behavior, where the curves approach the region in which $\vartheta < 0$ (highlighted as a pale red background). As we can see, even in that area $\vartheta > 0$ is satisfied.

APPENDIX E: IMPERFECT PHOTODETECTION AND HOMODYNE DETECTION

In this section, we investigate different sources of error that affect the protocols described in this paper. By using parameters taken from recent experimental benchmarks

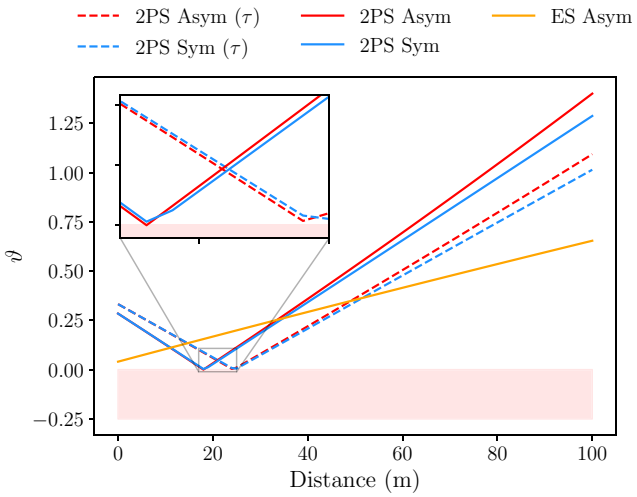

FIG. 12. Graphical representation of the curves constructed from Eq. (D5) against the traveled distance that, if positive, prove the submatrices used to compute this quantity characterize a covariance matrix, which satisfies a positivity condition, as well as the uncertainty principle. In orange, we represent the curve associated with the submatrices in Eqs. (39) that result from entanglement swapping. The blue and red solid curves correspond to the heuristic two-photon-subtracted "re-Gaussified" symmetric and asymmetric states, respectively, described in Eqs. (B17) and (B18). The blue and red dashed curves correspond to the probabilistic two-photon-subtracted "re-Gaussified" symmetric and asymmetric states, respectively, described in Eqs. (57) and (60). Inset: enlarged view of the region of short distances in which we observe that the condition $\vartheta > 0$ is still met.

in microwave quantum technologies, we are able to estimate how inefficiencies and imperfections surrounding microwave photocounting and homodyne detection affect photon subtraction, quantum teleportation, and entanglement swapping. We believe that this provides a closer relation to state-of-the-art experiments with quantum microwaves.

First, let us introduce a parameter for the efficiency of the microwave photodetectors. In Ref. [71], a circuit-QED-based microwave photon counter was presented, which could detect between zero and three photons, with fidelities ranging from 99% to 54%. Such a device is particularly useful for the photon-subtraction scheme investigated in the manuscript, in which we only consider single-photon subtraction in each mode of a bipartite entangled state. Then, we need to look at the success probability of detecting a single photon, which in this experiment is 76%. An imperfect detector can be modeled as a pure-loss channel, which is represented by a beam splitter that mixes the signal traveling towards the detector with a vacuum state, and whose transmissivity determines the efficiency. In this case, we have $\tau_{\text{detector}} = 0.76$. This characterizes the detection probability in the heuristic photon-subtraction case, but in the probabilistic description, this will be given by $\tau_{\text{total}} = \tau_{\text{detector}}\tau = 0.72$, since we have considered $\tau = 0.95$.

Taking into account the detector efficiency, we observe that the maximum negativity associated with the re-Gaussified photon-subtracted states is, at least, 47% of the maximum negativity of the photon-subtracted states with ideal detector efficiency. This means that, taking into account this source of error, the negativity of the states obtained through this entanglement distillation technique is almost cut in half. Furthermore, these values are below the negativity of the bare state in the ideal case, which means that performing photon subtraction leads to entanglement degradation. In order for it to be advantageous, with the parameters we have considered throughout this manuscript, we would need to have detection efficiencies above 85% for the heuristic protocol, and above 90% for the probabilistic one.

Now, let us discuss homodyne detection, a measurement technique that is widely used in many quantum communication protocols, and in this article is required for quantum teleportation and for entanglement swapping. Homodyne detection aims at extracting information about the quadratures of a signal by mixing it with a coherent light source with a large number of photons in a balanced beam splitter, and then measuring the photocurrents at both ends. From the difference between the currents, we can get information about either quadrature of the signal. This measurement works ideally if the source has an infinite number of photons (infinite gain), which is not generally the case. Therefore, we can consider the case of finite gain in homodyne detection.

The theoretical description of these measurements corresponds to a projection onto a state that is infinitely squeezed in x (or in p) in phase space. That is, an eigenstate of the position operator (or the momentum operator) whose eigenvalue corresponds to the signal's x (or p) quadrature value. In the symplectic formalism, this measurement operator has covariance matrix

$$\Gamma = \begin{pmatrix} e^{-2\xi} & 0 \\ 0 & e^{2\xi} \end{pmatrix} \equiv \begin{pmatrix} 1/\sqrt{G} & 0 \\ 0 & \sqrt{G} \end{pmatrix}. \tag{E1}$$

In the limit $G \to \infty$, we recover the usual homodyne detection scheme. Thus, the fidelity of teleporting an unknown coherent state with $|\theta|^2$ photons using a bipartite entangled state with covariance matrix

$$\Sigma = \begin{pmatrix} \alpha \mathbb{1}_2 & \gamma \sigma_z \\ \gamma \sigma_z & \beta \mathbb{1}_2 \end{pmatrix} \tag{E2}$$

is given by

$$\overline{F} = \frac{2(2+(1+\alpha)/\sqrt{G})}{4[1+(\alpha+\beta-2\gamma)/2]+[\alpha(5+\beta)+\beta-(\gamma-1)(\gamma+5)]/\sqrt{G}+2(1+\alpha)/G} \times \exp\left[-\frac{2(1-\alpha+\gamma)^2|\theta|^2/G}{[2+(1+\alpha)/\sqrt{G}][4(1+(\alpha+\beta-2\gamma)/2)+[\alpha(5+\beta)+\beta-(\gamma-1)(\gamma+5)]/\sqrt{G}+2(1+\alpha)/G]}\right]. \tag{E3}$$

In the limit $G \to \infty$ we recover $\overline{F} = (1+(\alpha+\beta-2\gamma)/2)^{-1}$, which is the usual result. Note that, while the average teleportation fidelity for an unknown coherent state with ideal homodyne detection does not depend on the value of the displacement for said state, we find that the first-order corrections do include this dependence in the value of θ. The average fidelity associated with a resource with increasing entanglement asymptotically tends to 1 when

considering ideal homodyne detection. In this case, it tends to the value $1/(1+1/\sqrt{G})$, which gets closer to 1 as G increases.

In a recent paper, continuous-variable quantum teleportation in the microwave regime was performed [10], where the optimal gain considered was 21 dB, which implies that $1/G \approx 0.008$. Using this value, and considering we want to teleport a vacuum state ($\theta = 0$), we observe that the fidelity reaches the maximum classical fidelity at 434 m for the asymmetric state, and at 429 m for the symmetric one, while this distance is 479 m with ideal homodyne detection for both kinds of state.

Here, we also consider the effect of finite-gain homodyne detection on the states that result from entanglement swapping. As a generalization of Eqs. (39), these states can be characterized by a covariance matrix with submatrices

$$\tilde{\Sigma}_A = \left(\alpha - \frac{\gamma^2(1+2\beta/\sqrt{G}+1/G)}{2[\beta+(1+\beta^2)/\sqrt{G}+\beta/G]}\right)\mathbb{1}_2, \quad \text{(E4a)}$$

$$\tilde{\Sigma}_D = \left(\alpha - \frac{\gamma^2(1+2\beta/\sqrt{G}+1/G)}{2[\beta+(1+\beta^2)/\sqrt{G}+\beta/G]}\right)\mathbb{1}_2, \quad \text{(E4b)}$$

$$\tilde{\varepsilon}_{AD} = \frac{\gamma^2(1-1/G)}{2[\beta+(1+\beta^2)/\sqrt{G}+\beta/G]}\sigma_z. \quad \text{(E4c)}$$

With entanglement swapping, the maximum classical fidelity is reached at 416 m, which is smaller than the reach of the bare states taking into account finite-gain homodyne detection. This is natural, since the effects of the finite gain come both from entanglement swapping and from quantum teleportation. Nevertheless, we have seen that finite-gain effects are not significantly detrimental to the measures we have computed in this manuscript, and this means that, if larger optimal gains can be engineered, errors can then be reduced. At the end of the day, we have observed that entanglement distillation and entanglement swapping suffer from errors associated with photon counting and homodyne detection. However, we believe that these errors can be easily overcome by technological improvements. Furthermore, by the time all the pieces necessary for experiments in open-air microwave quantum communication arrive, we expect these errors to be further reduced. Meanwhile, entanglement distribution and quantum teleportation with microwaves, in the realistic open-air scenario, are still viable despite the errors considered in this section.

[1] N. Gisin and R. Thew, Quantum communication, Nat. Photon. **1**, 165 (2007).

[2] Z.-S. Yuan, X.-H. Bao, C.-Y. Lu, J. Zhang, C.-Z. Peng, and J.-W. Pan, Entangled photons and quantum communication, Phys. Rep. **497**, 1 (2010).

[3] M. Krenn, M. Malik, T. Scheidl, R. Ursin, and A. Zeilinger, *Quantum Communication with Photons* (Optics in Our Time, Springer, Cham, 2016), p. 455.

[4] C. H. Bennett, G. Brassard, C. Crépeau, R. Jozsa, A. Peres, and W. K. Wootters, Teleporting an Unknown Quantum State via Dual Classical and Einstein-Podolsky-Rosen Channels, Phys. Rev. Lett. **70**, 1895 (1993).

[5] S. Pirandola, J. Eisert, C. Weedbrook, A. Furusawa, and S. L. Braunstein, Advances in quantum teleportation, Nat. Photon. **9**, 641 (2015).

[6] M. Baur, A. Fedorov, L. Steffen, S. Filipp, M. P. da Silva, and A. Wallraff, Benchmarking a Quantum Teleportation Protocol in Superconducting Circuits Using Tomography and an Entanglement Witness, Phys. Rev. Lett. **108**, 040502 (2012).

[7] L. Steffen, Y. Salathe, M. Oppliger, P. Kurpiers, M. Baur, C. Lang, C. Eichler, G. Puebla-Hellmann, A. Fedorov, and A. Wallraff, Deterministic quantum teleportation with feed-forward in a solid state system, Nature **500**, 319 (2013).

[8] S. L. Braunstein and H. J. Kimble, Teleportation of Continuous Quantum Variables, Phys. Rev. Lett. **80**, 869 (1998).

[9] S. Pirandola and S. Mancini, Quantum teleportation with continuous variables: A survey, Laser Phys. **16**, 1418 (2006).

[10] K. G. Fedorov, M. Renger, S. Pogorzalek, R. Di Candia, Q. Chen, Y. Nojiri, K. Inomata, Y. Nakamura, M. Partanen, A. Marx, R. Gross, and F. Deppe, Experimental quantum teleportation of propagating microwaves, Sci. Adv. **7**, eabk0891 (2021).

[11] E. Diamanti, H.-K. Lo, B. Qi, and Z. Yuan, Practical challenges in quantum key distribution, Npj Quantum Inf. **2**, 16025 (2016).

[12] L.-J. Wang, K.-Y. Zhang, J.-Y. Wang, J. Cheng, Y.-H. Yang, S.-B. Tang, D. Yan, Y.-L. Tang, Z. Liu, Y. Yu, Q. Zhang, and J.-W. Pan, Experimental authentication of quantum key distribution with post-quantum cryptography, Npj Quantum Inf. **7**, 67 (2021).

[13] C. H. Bennett and G. Brassard, Quantum cryptography: Public key distribution and coin tossing, Proc. IEEE Int. Conf. Comput. Syst. Signal Process. **175**, 8 (1984).

[14] A. K. Eckert, Quantum Cryptography Based on Bell's Theorem, Phys. Rev. Lett. **67**, 661 (1991).

[15] J. I. Cirac, P. Zoller, H. J. Kimble, and H. Mabuchi, Quantum State Transfer and Entanglement Distribution among Distant Nodes in a Quantum Network, Phys. Rev. Lett. **78**, 3221 (1997).

[16] C.-W. Chou, J. Laurat, H. Deng, K. S. Choi, H. de Riedmatten, D. Felinto, and H. J. Kimble, Functional quantum nodes for entanglement distribution over scalable quantum networks, Science **316**, 1316 (2007).

[17] L. Mišta, Jr. and N. Korolkova, Improving continuous-variable entanglement distribution by separable states, Phys. Rev. A **80**, 032310 (2009).

[18] J. Dias, M. S. Winnel, N. Hosseinidehaj, and T. C. Ralph, Quantum repeater for continuous-variable entanglement distribution, Phys. Rev. A **102**, 052425 (2020).

[19] H. J. Kimble, The quantum internet, Nature **453**, 1023 (2008).

[20] S. Wehner, D. Elkouss, and R. Hanson, Quantum internet: A vision for the road ahead, Science **362**, 6412 (2018).

[21] L. Gyongyosi and S. Imre, Opportunistic entanglement distribution for the quantum internet, Sci. Rep. **9**, 2219 (2019).

[22] T. Herbst, T. Scheidl, M. Fink, J. Handsteiner, B. Wittmann, R. Ursin, and A. Zeilinger, Teleportation of entanglement over 143 km, PNAS **112**, 6684 (2019).

[23] S. Wengerowsky, S. K. Joshi, F. Steinlechner, J. R. Zichi, S. M. Dobrovolskiy, R. van der Molen, J. W. N. Los, V. Zwiller, M. A. M. Versteegh, A. Mura, Davide Calonico, Massimo Inguscio, Hannes Hübel, Liu Bo Thomas Scheidl, Anton Zeilinger, André Xuereb, and Rupert Ursin, Entanglement distribution over a 96-km-long submarine optical fiber, PNAS **116**, 6684 (2019).

[24] J. Yin, Y. Cao, Y.-H. Li, S.-K. Liao, L. Zhang, J.-G. Ren, W.-Q. Cai, W.-Y. Liu, B. Li, and H. Dai *et al.*, Satellite-based entanglement distribution over 1200 kilometers, Science **356**, 1140 (2017).

[25] S.-K. Liao, W.-Q. Cai, W.-Y. Liu, L. Zhang, Y. Li, J.-G. Ren, J. Yin, Q. Shen, Y. Cao, and Z.-P. Li *et al.*, Satellite-to-ground quantum key distribution, Nature **549**, 43 (2017).

[26] S.-K. Liao, W.-Q. Cai, J. Handsteiner, B. Liu, J. Yin, L. Zhang, D. Rauch, M. Fink, J.-G. Ren, and W.-Y. Liu *et al.*, Satellite-Relayed Intercontinental Quantum Network, Phys. Rev. Lett. **120**, 030501 (2018).

[27] M. Minder, M. Pittaluga, G. L. Roberts, M. Lucamarini, J. F. Dynes, Z. L. Yuan, and A. J. Shields, Experimental quantum key distribution beyond the repeaterless secret key capacity, Nat. Photon. **13**, 334 (2019).

[28] D. Bouwmeester, J.-W. Pan, K. Mattle, M. Eibl, H. Weinfurter, and A. Zeilinger, Experimental quantum teleportation, Nature **390**, 575 (1997).

[29] A. Furusawa, J. L. Sørensen, S. L. Braunstein, C. A. Fuchs, H. J. Kimble, and E. S. Polzik, Unconditional quantum teleportation, Science **282**, 706 (1998).

[30] D. Boschi, S. Branca, F. De Martini, L. Hardy, and S. Popescu, Experimental Realization of Teleporting an Unknown Pure Quantum State via Dual Classical and Einstein-Podolsky-Rosen Channels, Phys. Rev. Lett. **80**, 1121 (1998).

[31] X.-M. Jin, J.-G. Ren, B. Yang, Z.-H. Yi, F. Zhou, X.-F. Xu, S.-K. Wang, D. Yang, Y.-F. Hu, S. Jiang, Tao Yang, Hao Yin, Kai Chen, Cheng-Zhi Peng, and Jian-Wei Pan, Experimental free-space quantum teleportation, Nat. Photon. **4**, 376 (2010).

[32] X.-S. Ma, T. Herbst, T. Scheidl, D. Wang, S. Kropatschek, W. Naylor, B. Wittmann, A. Mech, J. Kofler, E. Anisimova, Vadim Makarov, Thomas Jennewein, Rupert Ursin, and Anton Zeilinger, Quantum teleportation over 143 kilometres using active feed-forward, Nature **489**, 269 (2012).

[33] J.-G. Ren, P. Xu, H.-L. Yong, L. Zhang, S.-K. Liao, J. Yin, W.-Y. Liu, W.-Q. Cai, M. Yang, and L. Li *et al.*, Ground-to-satellite quantum teleportation, Nature **549**, 70 (2017).

[34] C. L. Degen, F. Reinhard, and P. Cappellaro, Quantum sensing, Rev. Mod. Phys. **89**, 035002 (2017).

[35] S. Pirandola, B. R. Bardhan, T. Gehring, C. Weedbrook, and S. Lloyd, Advances in photonic quantum sensing, Nat. Photon. **12**, 724 (2018).

[36] V. Giovannetti, S. Lloyd, and L. Maccone, Advances in quantum metrology, Nat. Photon. **5**, 222 (2011).

[37] E. Polino, M. Valeri, N. Spagnolo, and F. Sciarrino, Photonic quantum metrology, AVS Quantum Sci. **2**, 024703 (2020).

[38] S. Rodrigo, S. Abadal, E. Alarcón, and C. G. Almudever, *Will Quantum Computers Scale without Inter-Chip Comms? A Structured Design Exploration to the Monolithic vs Distributed Architectures Quest*, XXXV Conf. Design of Circuits and Integrated Systems (DCIS), (2020), p. 1.

[39] S. DiAdamo, M. Ghibaudi, and J. Cruise, Distributed quantum computing and network control for accelerated VQE, IEEE Trans. Quantum Eng. **2**, 3100921 (2021).

[40] The LIGO Scientific Collaboration, A gravitational wave observatory operating beyond the quantum shot-noise limit, Nat. Phys. **7**, 962 (2011).

[41] E. Oelker, T. Isogai, J. Miller, M. Tse, L. Barsotti, N. Mavalvala, and M. Evans, Audio-Band Frequency-Dependent Squeezing for Gravitational-Wave Detectors, Phys. Rev. Lett. **116**, 041102 (2016).

[42] M. A. Taylor and W. P. Bowen, Quantum metrology and its application in biology, Phys. Rep. **615**, 1 (2016).

[43] N. P. Mauranyapin, L. S. Madsen, M. A. Taylor, M. Waleed, and W. P. Bowen, Evanescent single-molecule biosensing with quantum-limited precision, Nat. Photon. **11**, 477 (2017).

[44] P.-A. Moreau, E. Toninelli, T. Gregory, and M. J. Padgett, Imaging with quantum states of light, Nat. Rev. Phys. **1**, 367 (2019).

[45] I. R. Berchera and I. P. Degiovanni, Quantum imaging with sub-Poissonian light: Challenges and perspectives in optical metrology, Metrologia **56**, 024001 (2019).

[46] M. Fink, F. Steinlechner, J. Handsteiner, J. P. Dowling, T. Scheidl, and R. Ursin, Entanglement-enhanced optical gyroscope, New J. Phys. **21**, 053010 (2019).

[47] R. Quan, Y. Zhai, M. Wang, F. Hou, S. Wang, X. Xiang, T. Liu, S. Zhang, and R. Dong, Demonstration of quantum synchronization based on second-order quantum coherence of entangled photons, Sci. Rep. **6**, 30453 (2016).

[48] B. D. Josephson, in *Superconductivity*, R. D. Parks, ed. (Marcel Dekker, New York, 1969).

[49] M. Büttiker, Zero-current persistent potential drop across small-capacitance Josephson junctions, Phys. Rev. B **36**, 3548 (1987).

[50] V. Bouchiat, D. Vion, P. Joyez, D. Esteve, and M. H. Devoret, Quantum coherence with a single Cooper pair, Phys. Scr. T76 (1998), p.165-70.

[51] J. Koch, T. M. Yu, J. Gambetta, A. A. Houck, D. I. Schuster, J. Majer, A. Blais, M. H. Devoret, S. M. Girvin, and R. J. Schoelkopf, Charge-insensitive qubit design derived from the Cooper pair box, Phys. Rev. A **76**, 042319 (2007).

[52] T. Yamamoto, K. Inomata, M. Watanabe, K. Matsuba, T. Miyazaki, W. D. Oliver, Y. Nakamura, and J. S. Tsai, Flux-driven Josephson parametric amplifier, Appl. Phys. Lett. **93**, 042510 (2008).

[53] M. A. Castellano-Beltran, K. D. Irwin, G. C. Hilton, L. R. Vale, and K. W. Lehnert, Amplification and squeezing of quantum noise with a tunable Josephson metamaterial, Nat. Phys. **4**, 929 (2008).

[54] C. J. Axline, L. D. Burkhart, W. Pfaff, M. Zhang, K. Chou, P. Campagne-Ibarcq, P. Reinhold, L. Frunzio, S. M. Girvin, L. Jiang, M. H. Devoret, and R. J. Schoelkopf, On-demand quantum state transfer and entanglement between remote microwave cavity memories, Nat. Phys. **14**, 705 (2018).

[55] P. Campagne-Ibarcq, E. Zalys-Geller, A. Narla, S. Shankar, P. Reinhold, L. Burkhart, C. J. Axline, W. Pfaff, L. Frunzio, R. J. Schoelkopf, and M. H. Devoret, Deterministic Remote Entanglement of Superconducting Circuits through Microwave Two-Photon Transitions, Phys. Rev. Lett. **120**, 200501 (2018).

[56] P. Kurpiers, P. Magnard, T. Walter, B. Royer, M. Pechal, J. Heinsoo, Y. Salathé, A. Akin, S. Storz, J.-C. Besse, S. Gasparinetti, A. Blais, and A. Wallraff, Deterministic quantum state transfer and remote entanglement using microwave photons, Nature **558**, 264 (2018).

[57] N. Leung, Y. Lu, S. Chakram, R. K. Naik, N. Earnest, R. Ma, K. Jacobs, A. N. Cleland, and D. I. Schuster, Deterministic bidirectional communication and remote entanglement generation between superconducting qubits, Npj Quant. Inf. **5**, 18 (2019).

[58] N. Roch, M. E. Schwartz, F. Motzoi, C. Macklin, R. Vijay, A. W. Eddins, A. N. Korotkov, K. B. Whaley, M. Sarovar, and I. Siddiqi, Observation of Measurement-Induced Entanglement and Quantum Trajectories of Remote Superconducting Qubits, Phys. Rev. Lett. **114**, 259901 (2015).

[59] A. Narla, S. Shankar, M. Hatridge, Z. Leghtas, K. M. Sliwa, E. Zalys-Geller, S. O. Mundhada, W. Pfaff, L. Frunzio, R. J. Schoelkopf, and M. H. Devoret, Robust Concurrent Remote Entanglement between Two Superconducting Qubits, Phys. Rev. X **6**, 031036 (2016).

[60] C. Dickel, J. J. Wesdorp, N. K. Langford, S. Peiter, R. Sagastizabal, A. Bruno, B. Criger, F. Motzoi, and L. DiCarlo, Chip-to-chip entanglement of transmon qubits using engineered measurement fields, Phys. Rev. B. **97**, 064508 (2018).

[61] P. Magnard, S. Storz, P. Kurpiers, J. Schär, F. Marxer, J. Lütolf, T. Walter, J.-C. Besse, M. Gabureac, K. Reuer, A. Akin, B. Royer, A. Blais, and A. Wallraff, Microwave Quantum Link between Superconducting Circuits Housed in Spatially Separated Cryogenic Systems, Phys. Rev. Lett. **125**, 260502 (2020).

[62] J. Goetz, S. Pogorzalek, F. Deppe, K. G. Fedorov, P. Eder, M. Fischer, F. Wulschner, E. Xie, A. Marx, and R. Gross, Photon Statistics of Propagating Thermal Microwaves, Phys. Rev. Lett. **118**, 103602 (2017).

[63] J. Goetz, F. Deppe, P. Eder, M. Fischer, M. Müting, J. P. Martínez, S. Pogorzalek, F. Wulschner, E. Xie, K. G. Fedorov, A. Marx, and R. Gross, Second-order decoherence mechanisms of a transmon qubit probed with thermal microwave states, Quantum Sci. Technol. **2**, 025002 (2017).

[64] M. Sanz, K. G. Fedorov, F. Deppe, and E. Solano, Challenges in Open-air Microwave Quantum Communication and Sensing, IEEE Conference on Antenna Measurements & Applications (CAMA), 1-4, (2018).

[65] M. Forsch, R. Stockill, A. Wallucks, I. Marinković, C. Gärtner, R. A. Norte, F. van Otten, A. Fiore, K. Srinivasan, and S. Gröblacher, Microwave-to-optics conversion using a mechanical oscillator in its quantum ground state, Nat. Phys. **16**, 69 (2020).

[66] A. Rueda, W. Hease, S. Barzanjeh, and J. M. Fink, Electro-optic entanglement source for microwave to telecom quantum state transfer, Npj Quantum Inf. **5**, 108 (2019).

[67] K. G. Fedorov, L. Zhong, S. Pogorzalek, P. Eder, M. Fischer, J. Goetz, E. Xie, F. Wulschner, K. Inomata, T. Yamamoto, Y. Nakamura, R. Di Candia, U. Las Heras, M. Sanz, E. Solano, E. P. Menzel, F. Deppe, A. Marx, and R. Gross, Displacement of Propagating Squeezed Microwave States, Phys. Rev. Lett. **117**, 020502 (2016).

[68] S. Pogorzalek, K. G. Fedorov, M. Xu, A. Parra-Rodriguez, M. Sanz, M. Fischer, E. Xie, K. Inomata, Y. Nakamura, E. Solano, A. Marx, F. Deppe, and R. Gross, Secure quantum remote state preparation of squeezed microwave states, Nat. Commun. **10**, 2604 (2019).

[69] K. G. Fedorov, S. Pogorzalek, U. Las Heras, M. Sanz, P. Yard, P. Eder, M. Fischer, J. Goetz, E. Xie, K. Inomata, Y. Nakamura, R. Di Candia, E. Solano, A. Marx, F. Deppe, and R. Gross, Finite-time quantum entanglement in propagating squeezed microwaves, Sci. Rep. **8**, 6416 (2018).

[70] R. Di Candia, K. G. Fedorov, L. Zhong, S. Felicetti, E. P. Menzel, M. Sanz, F. Deppe, A. Marx, R. Gross, and E. Solano, Quantum teleportation of propagating quantum microwaves, EPJ Quantum Technol. **2**, 25 (2015).

[71] R. Dassonneville, R. Assouly, T. Peronnin, P. Rouchon, and B. Huard, Number-Resolved Photocounter for Propagating Microwave Mode, Phys. Rev. Appl. **14**, 044022 (2020).

[72] S. Pirandola, Satellite quantum communications: Fundamental bounds and practical security, Phys. Rev. Res. **3**, 023130 (2021).

[73] S. Pirandola, Limits and security of free-space quantum communications, Phys. Rev. Res. **3**, 013279 (2021).

[74] Arvind, B. Dutta, N. Mukunda, and R. Simon, The real symplectic groups in quantum mechanics and optics, Pramana **45**, 471 (1995).

[75] J. Williamson, On the algebraic problem concerning the normal forms of linear dynamical systems, Am. J. Math **58**, 141 (1936).

[76] J. Williamson, On the normal forms of linear canonical transformations in dynamics, Am. J. Math **59**, 599 (1937).

[77] J. Williamson, The exponential representation of canonical matrices, Am. J. Math **61**, 897 (1939).

[78] L. Vaidman, Teleportation of quantum states, Phys. Rev. A **49**, 1473 (1994).

[79] S. L. Braunstein and P. van Loock, Quantum information with continuous variables, Rev. Mod. Phys. **77**, 513 (2005).

[80] A. Serafini, *Quantum Continuous Variables* (CRC Press, Taylor & Francis Group, LLC, Boca Raton, 2017).

[81] C. Weedbrook, S. Pirandola, R. García-Patrón, N. J. Cerf, T. C. Ralph, J. H. Shapiro, and S. Lloyd, Gaussian quantum information, Rev. Mod. Phys. **84**, 621 (2012).

[82] G. J. Milburn and S. L. Braunstein, Quantum teleportation with squeezed vacuum states, Phys. Rev. A **60**, 937 (1999).

[83] T. Opatrný, G. Kurizki, and D.-G. Welsch, Improvement on teleportation of continuous variables by photon subtraction via conditional measurement, Phys. Rev. A **61**, 032302 (2000).

[84] P. T. Cochrane, T. C. Ralph, and G. J. Milburn, Teleportation improvement by conditional measurements on the two-mode squeezed vacuum, Phys. Rev. A **65**, 062306 (2002).

[85] P. Marian and T. A. Marian, Continuous-variable teleportation in the characteristic-function description, Phys. Rev. A **74**, 042306 (2006).

[86] T. Gonzalez-Raya and M. Sanz, Coplanar antenna design for microwave entangled signals propagating in open air, Quantum **6**, 783 (2022).

[87] L. Zhong, E. P. Menzel, R. Di Candia, P. Eder, M. Ihmig, A. Baust, M. Haeberlein, E. Hoffmann, K. Inomata, and T. Yamamoto, Squeezing with a flux-driven Josephson parametric amplifier, New J. Phys. **15**, 125013 (2013).

[88] S. Pogorzalek, K. G. Fedorov, L. Zhong, J. Goetz, F. Wulschner, M. Fischer, P. Eder, E. Xie, K. Inomata, and T. Yamamoto *et al.*, Hysteretic Flux Response and Nondegenerate Gain of Flux-Driven Josephson Parametric Amplifiers, Phys. Rev. Appl. **8**, 024012 (2017).

[89] M. Renger, S. Pogorzalek, Q. Chen, Y. Nojiri, K. Inomata, Y. Nakamura, M. Partanen, A. Marx, R. Gross, F. Deppe, and K. G. Fedorov, Beyond the standard quantum limit of parametric amplification, arXiv:2011.00914 (2020) .

[90] S. Boutin, D. M. Toyli, A. V. Venkatramani, A. W. Eddins, I. Siddiqi, and A. Blais, Effect of Higher-Order Nonlinearities on Amplification and Squeezing in Josephson Parametric Amplifiers, Phys. Rev. Appl. **8**, 054030 (2017).

[91] C. M. Ho, C. Wang, K. Angkasa, and K. Gritton, *Estimation of Microwave Power Margin Losses Due to Earth's Atmosphere and Weather in the Frequency Range of 3–30 GHz* (Jet Propulsion Laboratory, California Institute of Technology, 2004).

[92] *Attenuation by atmospheric gases and related effects*, ITU-R P.676-12 (2019).

[93] T. C. Ralph and A. P. Lund, Nondeterministic noiseless linear amplification of quantum systems, AIP Conf. Proc. **1110**, 155 (2009).

[94] G. Y. Xiang, T. C. Ralph, A. P. Lund, N. Walk, and G. J. Pryde, Noiseless linear amplification and distillation of entanglement, Nat. Photon. **4**, 316 (2010).

[95] D. T. Pegg, L. S. Phillips, and S. M. Barnett, Optical State Truncation by Projection Synthesis, Phys. Rev. Lett. **81**, 1604 (1998).

[96] D. E. Browne, J. Eisert, S. Scheel, and M. B. Plenio, Driving non-Gaussian to Gaussian states with linear optics, Phys. Rev. A **67**, 062320 (2003).

[97] J. Fiurášek, Distillation and purification of symmetric entangled Gaussian states, Phys. Rev. A **82**, 042331 (2010).

[98] J. Eisert, D. E. Browne, S. Scheel, and M. B. Plenio, Distillation of continuous-variable entanglement with optical means, Ann. Phys. **311**, 431 (2004).

[99] H. Takahashi, J. S. Neergaard-Nielsen, M. Takeuchi, M. Takeoka, K. Hayasaka, A. Furusawa, and M. Sasaki, Entanglement distillation from Gaussian input states, Nat. Photon. **4**, 178 (2010).

[100] J. Hoelscher-Obermaier and P. van Loock, Optimal Gaussian entanglement swapping, Phys. Rev. A **83**, 012319 (2011).

[101] R. Lescanne, S. Deléglise, E. Albertinale, U. Réglade, T. Capelle, E. Ivanov, T. Jacqmin, Z. Leghtas, and E. Flurin, Irreversible Qubit-Photon Coupling for the Detection of Itinerant Microwave Photons, Phys. Rev. X **10**, 021038 (2020).

[102] S. Kono, K. Koshino, Y. Tabuchi, A. Noguchi, and Y. Nakamura, Quantum non-demolition detection of an itinerant microwave photon, Nat. Phys. **14**, 546 (2018).

[103] J.-C. Besse, S. Gasparinetti, M. C. Collodo, T. Walter, P. Kurpiers, M. Pechal, C. Eichler, and A. Wallraff, Single-Shot Quantum Nondemolition Detection of Individual Itinerant Microwave Photons, Phys. Rev. X **8**, 021003 (2018).

[104] C. Eichler, D. Bozyigit, and A. Wallraff, Characterizing quantum microwave radiation and its entanglement with superconducting qubits using linear detectors, Phys. Rev. A **86**, 032106 (2012).

[105] J. S. Sidhu, S. K. Joshi, M. Gündoğan, T. Brougham, D. Lowndes, L. Mazzarella, M. Krutzik, S. Mohapatra, D. Dequal, and G. Vallone *et al.*, Advances in space quantum communications, IET Quant. Comm. **2**, 182 (2021).

[106] H. T. Friis, A note on a simple transmission formula, Proc. I.R.E. Waves Electrons **34**, 254 (1946).

[107] D. C. Hogg, Fun with the Friis free-space transmission formula, IEEE Antennas Propag. Mag. **35**, 33 (1993).

[108] J. A. Shaw, Radiometry and the Friis transmission equation, Am. J. Phys. **81**, 33 (2013).

[109] C. A. Balanis, *Antenna Theory: Analysis and Design, 3rd Edition* (John Wiley and sons, Hoboken, 2005).

[110] A. A. Clerk, M. H. Devoret, S. M. Girvin, F. Marquardt, and R. J. Schoelkopf, Introduction to quantum noise, measurement, and amplification, Rev. Mod. Phys. **82**, 1155 (2010).